



Isoprene photo-oxidation products quantify the effect of pollution on hydroxyl radicals over Amazonia

Y. Liu, S. Springston

To be published in "Science Advances"

April 2018

Environmental and Climate Sciences Department

Brookhaven National Laboratory

U.S. Department of Energy

USDOE Office of Science (SC), Biological and Environmental Research (BER) (SC-23)

Notice: This manuscript has been authored by employees of Brookhaven Science Associates, LLC under Contract No. DE-SC0012704 with the U.S. Department of Energy. The publisher by accepting the manuscript for publication acknowledges that the United States Government retains a non-exclusive, paid-up, irrevocable, world-wide license to publish or reproduce the published form of this manuscript, or allow others to do so, for United States Government purposes.

DISCLAIMER

This report was prepared as an account of work sponsored by an agency of the United States Government. Neither the United States Government nor any agency thereof, nor any of their employees, nor any of their contractors, subcontractors, or their employees, makes any warranty, express or implied, or assumes any legal liability or responsibility for the accuracy, completeness, or any third party's use or the results of such use of any information, apparatus, product, or process disclosed, or represents that its use would not infringe privately owned rights. Reference herein to any specific commercial product, process, or service by trade name, trademark, manufacturer, or otherwise, does not necessarily constitute or imply its endorsement, recommendation, or favoring by the United States Government or any agency thereof or its contractors or subcontractors. The views and opinions of authors expressed herein do not necessarily state or reflect those of the United States Government or any agency thereof.

FRONT MATTER

Full Title

Isoprene photo-oxidation products quantify the effect of pollution on hydroxyl radicals over Amazonia

Short Title

Effect of pollution on OH radicals

Authors

Yingjun Liu, † Roger Seco, 2 Saewung Kim, 2 Alex B. Guenther, 2 Allen H. Goldstein, 3 Frank N. Keutsch, 1,4 Stephen R. Springston, 5 Thomas B. Watson, 5 Paulo Artaxo, 6 Rodrigo A. F. Souza, 7 Karena A. McKinney, 1, and Scot T. Martin 1,8*

Affiliations

- ¹ School of Engineering and Applied Sciences, Harvard University, Cambridge, Massachusetts, United States.
- ² Department of Earth System Science, University of California, Irvine, California, United States.
- ³ Department of Environmental Science, Policy and Management, University of California, Berkeley, California, United States.
- ⁴ Department of Chemistry and Chemical Biology, Harvard University, Cambridge, Massachusetts, United States.
- ⁵ Department of Environmental and Climate Sciences, Brookhaven National Laboratory, Upton, New York, United States.
- ⁶ Department of Applied Physics, University of São Paulo, São Paulo, Brazil.
- ⁷ Department of Meteorology, Amazonas State University, Manaus, Amazonia, Brazil.
- ⁸ Department of Earth and Planetary Sciences, Harvard University, Cambridge, Massachusetts, United States.
- † Now at Department of Environmental Science, Policy and Management, University of California, Berkeley, California, United States
- ‡ Now at Department of Chemistry, Colby College, Waterville, Maine, United States
- * To whom correspondence should be addressed. E-mail: scot_martin@harvard.edu, kamckinney@seas.harvard.edu

Journal

Science Advances

Abstract

1

- Nitrogen oxides (NO_x) emitted from human activities are believed to regulate the atmospheric
- 3 oxidation capacity of the troposphere. Observational evidence, however, is limited for the low-
- 4 to-median NO_x concentrations prevalent outside of polluted regions. Directly measuring
- 5 oxidation capacity, represented primarily by hydroxyl radicals (OH), is challenging, and the span
- 6 in NO_x concentrations at a single observation site is often not wide. Herein, concentrations of
- 7 isoprene and its photo-oxidation products were used to infer the equivalent noontime OH
- 8 concentrations. The fetch at an observation site in central Amazonia experienced varied
- 9 contributions from background regional air, urban pollution, and biomass burning. The afternoon
- 10 concentrations of reactive nitrogen oxides (NO_v), indicative of NO_x exposure during the
- preceding few hours, spanned from 0.3 to 3.5 ppb. Accompanying the increase of NO_v
- concentration, the inferred equivalent noontime OH concentrations increased by at least 250%,
- from 0.6 to 1.6×10^6 cm⁻³. The conclusion is that, compared to background conditions of low
- NO_x concentrations over the Amazon forest, pollution increased NO_x concentrations and
- amplified OH concentrations, indicating the susceptibility of the atmospheric oxidation capacity
- over the forest to anthropogenic influence and reinforcing the important role of NO_x in sustaining
- 17 OH concentrations.

MAIN TEXT

Introduction

The Earth's atmosphere is an oxidizing medium that drives organic molecules toward
carbon dioxide, and oxidation by hydroxyl radicals (OH) initiates the majority of these reactions
(1, 2). Oxidation by OH radicals also leads to the production of many secondary pollutants that
affect human health and climate, such as organic particulate matter and ozone. In relation to OH
concentrations, the NO_x family, defined as including nitric oxide (NO) and nitrogen dioxide
(NO ₂), has two roles (2). The chemistry is illustrated in Figure 1a. On the one hand, NO reacts
with hydroperoxyl radicals (HO ₂) and organic peroxyl radicals (RO ₂) to produce OH
catalytically in the presence of sunlight, thereby enhancing OH concentrations. On the other
hand, at higher NO_x concentrations, the direct reaction of NO_2 with OH to produce nitric acid
(HNO ₃) becomes dominant, and NO _x serves as an OH sink. Hydroxyl radical concentrations thus
increase as NO_x concentrations increase below a threshold NO_x concentration, and they decrease
as NO_x concentrations increase above this threshold. The net result is that OH concentrations
follow a bell curve with respect to NO_x concentration, as illustrated in Figure 1b (2, 3).
The applicability of this classical understanding of $OH-NO_x$ chemistry, as represented by
the bell curve, to atmospheric conditions is under challenge based on field measurements of OH
concentrations in regions where volatile organic compounds (VOCs) are abundant. A meta-study
examined the dependence of OH concentrations across a broad range of NO_x conditions (4). The
observations ranged from tropical forests in South America and Southeast Asia (5, 6), to
deciduous forest in US and rural area in China (7-9), to polluted metropolitan regions of New
York City, Beijing, Tokyo, and Mexico City ($10-13$). Above a threshold NO _x concentration, OH
concentrations decreased with increasing NO_x concentration, as expected. Below the threshold
NO _x concentration, however, reported OH concentrations in many regions were unexpectedly

high, and collectively they appeared to be independent of NO_x concentration, as illustrated by the horizontal line in Figure 1b.

42

43

44

45

46

47

48

49

50

51

52

53

54

55

56

57

58

59

60

61

62

63

64

Possible mechanisms for maintaining elevated OH concentrations under atmospheric conditions with below-threshold NO_x concentrations, have been considered (7, 14-16). In regions where VOCs are abundant, especially over and downwind of forests, the major fate of OH is reaction with biogenic VOCs to produce RO₂. Possible reactions of RO₂ radicals to regenerate OH and thereby maintain OH concentrations have been suggested, especially for forested regions dominated by isoprene emissions, such as OH production from the reaction of HO₂ with isoprene-derived RO₂ radicals (ISOPOO) (14, 17) as well as OH release following ISOPOO isomerization (16, 18). Even so, these mechanisms appear insufficient to quantitatively explain the reported high OH concentrations at low NO_x concentrations (14, 17, 18). Alternatively, the accuracy of reports of high OH concentrations is uncertain because of the possibility of interferences in the underlying measurement technique of Laser Induced Fluorescence (LIF) (9, 19, 20). For instance, Mao et al. (9) attributed 40 to 60% of the nominal OH signal observed in a California forest to interferences. After correction, the data fell on the bell curve, instead of on the horizontal line of Figure 1b (4). Up to now, there is no consensus on whether similar interferences may have occurred in the other measurements included in the meta-study. The LIF instruments are custom built in variable configurations by different research groups. Another uncertainty related to the meta-study is that the span in NO_x concentration of each underlying study was usually not wide, so no individual study closely tested the response of OH concentration to NO_x concentration across a broad range. Instead, the analysis in the metastudy was based on normalization of observations across multiple sites, different instruments, and differing atmospheric conditions. In short, possible new mechanisms for OH production and

recycling under atmospheric conditions and possible artifacts in the underlying data sets all remain to be reconciled.

Herein, a complementary approach based on isoprene photo-oxidation products is presented for mapping the dependence of OH concentration on NO_x concentration for atmospheric conditions over an isoprene-dominated forested environment. Precedent approaches for estimating OH concentrations include the use of a range of OH-reacting trace species as well as OH reaction products and their ratios (3, 21–24). Isoprene is the dominant VOC emitted to the atmosphere from many forests (25), and reaction with OH is its primary loss pathway (26). As OH concentration increases, the concentration $C_{\rm ISOP}$ of isoprene decreases, and the sum concentration $C_{\rm PROD}$ of its oxidation products increases, provided that other factors such as reaction time, ozone concentration, and isoprene emission rates are unchanged. The presentation herein develops an analysis to employ the afternoon parent-to-product concentration ratio $C_{\rm ISOP}/C_{\rm PROD}$ to infer equivalent noontime OH concentration within an air mass during the preceding daylight hours. The analysis must account for several factors, in addition to OH concentration, that influence $C_{\rm ISOP}/C_{\rm PROD}$.

Data sets were recorded at a single site in the *Observations and Modeling of the Green Ocean Amazon* (GoAmazon2014/5) Experiment in central Amazonia during the wet and dry seasons of 2014 (27). At different times, the sampling site received mixtures to various degrees of unpolluted regional background air, air influenced by regional fires (especially in the dry season), or air that had passed over the nearby city of Manaus, an urban region of 2 million inhabitants and a strong regional source of NO_x . The site was 4 to 6 h downwind from Manaus for the typical prevailing easterlies associated with trade winds (27, 28). As a result, the GoAmazon2014/5 data sets spanned a great breadth of upwind NO_x chemistry at a single

observation site (29). The range in measured isoprene concentrations was similar to that of the forested sites of the meta-study (4). The GoAmazon2014/5 data sets were used in the analysis herein to strongly test for a bell curve versus a horizontal line in the response of OH concentration to NO_x concentration in an isoprene-dominated forested environment (Figure 1b).

Results

The median and interquartile ranges of measured $C_{\rm ISOP}$ and $C_{\rm PROD}$ are plotted by hour in Figures 2a and 2b. The dry and wet season data sets are represented by red and blue coloring, respectively. The product concentration $C_{\rm PROD}$ represents the sum concentration of methyl vinyl ketone (MVK, C_4H_6O), methacrolein (MACR; C_4H_6O), and isoprene-derived hydroperoxide isomers (including (1,2)-ISOPOOH, (4,3)-ISOPOOH, hereafter ISOPOOH; $C_5H_{10}O_3$). MVK and MACR are the major OH-reaction products of isoprene along NO-mediated pathways (17). The ISOPOOH species are the major products along HO_2 -mediated pathways (30). Although the relative importance of the NO and HO_2 pathways varies with NO_x concentration (29), the summed production yield of MVK, MACR and ISOPOOH is approximately 70% across the atmospherically relevant range of NO_x concentrations (30).

Figures 2a and 2b show that before sunrise $C_{\rm ISOP}$ and $C_{\rm PROD}$ were <20% and <10% of their respective afternoon values. At sunrise, the forest began to emit isoprene, and photochemical production of OH also began. Isoprene had lifetime of 2.8 hours against OH attack for $C_{\rm OH} = 1.0 \times 10^6$ cm⁻³, whereas the lifetimes of products against chemical loss were up to 5 times higher. In line with these processes, Figures 2a and 2b show that at sunrise $C_{\rm ISOP}$ increased, followed shortly thereafter by increases in $C_{\rm PROD}$. Isoprene also reacted with photochemically produced O₃, but this pathway was typically one order of magnitude less important than the OH pathway for the prevailing atmospheric conditions (26). The resulting

MVK and MACR was a minor contribution to the overall production of these species. In addition to chemical loss and production, $C_{\rm ISOP}$ and $C_{\rm PROD}$ were also affected by dry and wet deposition as well as by entrainment of air from above the boundary layer. The analysis herein focuses on afternoon concentrations $C_{\rm ISOP}$ and $C_{\rm PROD}$ because that OH oxidation has greatest impact on $C_{\rm ISOP}$ and $C_{\rm PROD}$ at this time of the day. In addition, the possibility of intercepting a polluted air mass from Manaus was highest in the afternoon given that the research site was 4 to 6 h downwind of this pollution source for typical winds following sunrise (28).

Scatter plots for the afternoon hours (13:00-16:00 local time) of $C_{\rm ISOP}$, $C_{\rm PROD}$, and

111

112

113

114

115

116

117

118

119

120

121

122

123

124

125

126

127

128

129

130

131

132

133

 C_{PROD}/C_{ISOP} in relation to the sum concentration C_{NO_y} of reactive nitrogen species (NO_y) are shown in Figures 3a, 3b, and 3c, respectively. In addition to the NO_x species, the NO_y family also included reservoir forms of oxidized nitrogen like HNO₃ that were products of atmospheric reactions of $NO_x(3)$. A few hours downwind of the Manaus source region at the observation site, $C_{\text{NO}_{v}}$ remained a semi-conserved quantity whereas $C_{\text{NO}_{v}}$ had significantly decreased. Atmospheric conversion of NO_x to NO_y also occurred for air masses downwind of regional biomass burning. Therefore, for the analysis, C_{NO_v} was employed to represent the integrated intensity of NO_x chemistry prior to arrival of an air mass at the observation site (29, 31). The ratio $C_{\text{NO}}/C_{\text{NO}}$, had interquartile variability of 0.30 to 0.44 across the study period, supporting the use of the simplified representation $C_{NO_{v}}$. As shown in Figure 3, the hourly-averaged afternoon values of C_{NO_v} spanned more than one order of magnitude from 0.3 ppb to 3.5 ppb. The inter-quartile range of $C_{NO_{\nu}}$ in the afternoon hours was 0.7 to 1.2 ppb in the wet season and 1.3 to 2.0 ppb in the dry season. As a reference point, C_{NO_y} for regional background conditions was 0.46 ± 0.26 ppb (32). Concentrations above 1 ppb at the observation site indicated the effects of Manaus pollution or regional biomass burning (29, 31).

The scatter plots of Figure 3 illustrate the following findings. $C_{\rm ISOP}$ did not correlate with $C_{\rm NO_y}$ (Spearman's rank p of 0.4 and correlation coefficient r of -0.07; Figure 3a). $C_{\rm PROD}$ did correlate with $C_{\rm NO_y}$ ($p < 10^{-4}$; Figure 3b), yet the data were scattered (r = 0.4). By comparison, the ratio $C_{\rm PROD}/C_{\rm ISOP}$ correlated tightly with $C_{\rm NO_y}$ ($p < 10^{-4}$ and r = 0.6; Figure 3c). The median of $C_{\rm PROD}/C_{\rm ISOP}$ increased from 0.4 to 1.0 as $C_{\rm NO_y}$ changed from below 0.5 ppb to above 2 ppb. A high value of $C_{\rm PROD}/C_{\rm ISOP}$ was never observed for a low value of $C_{\rm NO_y}$ (Figure 3c).

An unclear trend in the concentration plots on the one hand (Figures 3a and 3b) compared to a clear trend in the ratio plot on the other hand (Figure 3c) with respect to C_{NO_y} can be explained by the large temporal variability in isoprene emissions (22). This variability was independent of C_{NO_y} and thus confounded direct relationships between C_{ISOP} and C_{NO_y} or C_{PROD} and C_{NO_y} . By comparison, the ratio $C_{\text{PROD}}/C_{\text{ISOP}}$ largely compensated the variability in isoprene emissions and thereby revealed differences in atmospheric oxidation. For these reasons, $C_{\text{PROD}}/C_{\text{ISOP}}$ was used in the further analysis herein focused on understanding and quantifying the effects of pollution on the atmospheric oxidation cycle over central Amazonia.

Discussion

Relating OH concentration to the ratio C_{PROD}/C_{ISOP}

A model of isoprene photochemistry over the course of one day was constrained by the observed values of C_{PROD}/C_{ISOP} to estimate the equivalent noontime OH concentration for the preceding daytime hours upwind of the observation site, as follows. For products species i of isoprene oxidation, where i is one of (1,2)-ISOPOOH, (4,3)-ISOPOOH, MVK, or MACR, the time course of product concentrations $C_i(t)$ in an air mass is governed by the following family of equations:

156
$$\frac{dC_i}{dt} = y_i(\text{NO}) k_{\text{ISOP,OH}} C_{\text{OH}}(t) C_{\text{ISOP}}(t) + y_{i,O_3} k_{\text{ISOP,O}_3} C_{O_3}(t) C_{\text{ISOP}}(t) - k_i(t) C_i(t), \qquad (1)$$

where y_i is the production yield of product species i from the reaction between hydroxy radical and isoprene. It varies according to the fate of ISOPOO, which is largely controlled by the NO concentration and hence susceptible to pollution. $C_{OH}(t)$, $C_{ISOP}(t)$, and $C_{O3}(t)$, where t represents time, are the concentrations of hydroxyl radical, isoprene, and ozone, respectively, all of which vary strongly with time of day. $k_{ISOP,OH}$ and $k_{ISOP,O3}$ are the reaction rate constants of isoprene with hydroxyl radical and ozone, respectively. $y_{i,O3}$ is the production yield of product species i from the reaction between ozone and isoprene (30). k_i is a composite, pseudo-first order loss coefficient of species i, given by $k_i(t) = k_{i,OH} C_{OH}(t) + k_{i,O3} C_{O3}(t) + k_{i,en} + k_{i,de}$ for bimolecular reaction between species i and OH or O₃, entrainment mixing with air above the boundary layer (en), and deposition to the planetary surface (de). Supplementary Table S1 lists values of $y_{i,O3}$, $k_{i,OH}$, and $k_{i,O3}$ as well as typical values of $k_{i,en}$ and $k_{i,de}$ for central Amazonia, partly reproduced from Liu et al. (29). For comparison, a more detailed model for entrainment to couple chemistry and boundary layer dynamics was also explored, and similar results were obtained (cf. Supplementary Materials).

The text below first discusses the Sequential Reaction Model (SRM), which is a commonly used simplification of Equation (1) to relate an observed ratio $C_{\text{PROD}}/C_{\text{ISOP}}$ to an inferred OH concentration (21). The conclusion reached is that the SRM is not appropriate for analysis of the collected data set. The text then introduces a complementary approach based on (i) time-dependent approximations of C_{ISOP} , C_{OH} , and C_{O3} and (ii) substitution of the production yield $y_i(\text{NO})$ by an effective production yield denoted by $y_i^* \left(C_{\text{NO}_y} \right)$.

Analysis by SRM assumes that isoprene emissions can be taken as a point source (typically an upwind forest) and that isoprene is subsequently oxidized during transport to an observation site. More specifically, isoprene is not emitted into the air parcel along its path of travel, and reaction with OH is the dominant process governing the time evolution of $C_{\rm ISOP}$ (i.e., $dC_{\rm ISOP}/dt = -k_{\rm ISOP,OH} C_{\rm OH} C_{\rm ISOP}$). Other assumptions include constant $C_{\rm OH}$ and $C_{\rm O_3}$, a fixed $y_{\rm i}$, a fixed reaction time t, and negligible entrainment and deposition. For these conditions, Equation (1) transforms to an explicit relation that allows $C_{\rm OH}$ to be inferred from measured $C_{\rm PROD}/C_{\rm ISOP}$ (21). The major underlying SRM assumption of an upwind point source was, however, not applicable to the GoAmazon2014/5 scenario. The observation site was surrounded by forest for hundreds of km, meaning that isoprene was continuously emitted into air parcels throughout transport, and $C_{\rm ISOP}$ and $C_{\rm PROD}$ corresponded to the integrated balance between source and loss processes throughout transport.

An alternative scheme to the SRM is developed herein to constrain C_{OH} based on observed C_{PROD}/C_{ISOP} . The regional area around T3 is approximated as a homogeneous forest representing a perfectly diffuse non-point source region of isoprene. Analysis using Google Earth shows that surface forest coverage exceeded 70% in a 100 km radius for the dominating easterlies and northeasterlies in the wind rose and greater than 80% for all directions (33). The radius of 100 km was based on typical wind speeds of 10 to 20 km h⁻¹ and the time period from the start of photochemistry at daybreak to the analysis window in the afternoon. Within this 100-km radius, the forest type and hence isoprene emissions varied to some extent (34), and there were also scattered pastures, two large rivers, and the urban area of Manaus. These factors notwithstanding, a homogeneous diffuse source of isoprene emissions was taken as an acceptable approximation for the accuracy of the modeling herein.

Under this approach of a homogeneous source region, a time series of observations at a Eulerian point is fully transformable into a Lagrangian model of a time series of concentrations within an air parcel over the course of a time period (35, 36). Equation (1) describes the transformations of product species C_i within the Lagrangian parcel, and in the treatment herein observations constrained the terms. For instance, measurements of the time course of isoprene concentrations directly constrained $C_{\text{ISOP}}(t)$. Steady increases were observed from sunrise to midafternoon (Figure 2a), and the observed time dependence was represented empirically by the following linear equation:

208
$$C_{ISOP}(t) = \xi C_{ISOP,0} \left(1 + t/t_{ISOP}^*\right),$$
 (2)

where ξ was a daily scaling factor representing the variability in isoprene concentrations for each day, $C_{\rm ISOP,0}$ was the typical isoprene concentration at time zero (sunrise), and $t_{\rm ISOP}^*$ was the typical characteristic time for $C_{\rm ISOP}$ to double its initial value. A value of 2.5 h for $t_{\rm ISOP}^*$ represented most days. Values of $C_{\rm ISOP,0}$ of 0.35 and 0.6 ppb were used as approximate values to represent the wet and dry seasons, respectively. Equation (2) is plotted in Figure 2a as the black dashed lines to represent median $C_{\rm ISOP}(t)$ from sunrise to midafternoon in the two seasons using ξ of unity. The analysis below further shows that the quantities ξ and $C_{\rm ISOP,0}$ drop out (cf. Equation (5)) so that the actual values are not important.

In regard to $C_{OH}(t)$, hydroxyl radical concentrations strongly correlate with the photolysis frequency J_{O_3} of ozone for most locations worldwide (37). In the analysis, the daily course of hydroxyl radical concentrations was approximated as an equivalent noontime concentration $C_{OH,noon}$ modulated by a time-dependent photolysis frequency J_{O_3} of ozone along the $O(^1D)$ channel, as follows:

222
$$C_{\text{OH}}(t) = C_{\text{OH,noon}} \frac{J_{O_3}(t)}{J_{O_3 \text{ noon}}},$$
 (3)

where $J_{\rm O_3,noon}$ was the peak value occurring at local noon for the equatorial location. The variation of $J_{\rm O_3}(t)/J_{\rm O_3,noon}$ followed that of the Master Chemical Mechanism for clear skies at the latitude and longitude of the observation site (30) (cf. Figure S2). The value of $C_{\rm OH,noon}$ was not known prior to the analysis, and inferring its value was a main point of the analysis presented herein.

The production yield $y_i(\rm NO)$ in Equation (1), written in full form as $y_i(C_{\rm NO}(t))$, does not fulfill the homogeneity requirement of a Eulerian-to-Lagrangian transformation because of the

fulfill the homogeneity requirement of a Eulerian-to-Lagrangian transformation because of the decreasing concentration of NO along the path. Observations and analysis presented in ref (29) for this same observation site showed that the ratio of product concentrations

 $C_{\text{ISOPOOH}}/C_{\text{MVK+MACR}}$ correlated tightly with C_{NO_y} , and this ratio was further transformed in that study to the effective production ratio $y^*_{\text{ISOPOOH}}/y^*_{\text{MVK+MACR}}$ by combining the measurements with kinetic modeling (29). Herein the production yield $y_i(C_{\text{NO}}(t))$ in the Lagrangian framework was substituted by an empirical effective production yield $y^*_i(C_{\text{NO}_y})$. The relationship $y^*_i(C_{\text{NO}_y})$ is presented in Figure S3 (see further in Supplementary Materials). This treatment subsumed the reality of a detailed history of NO exposure within the sampled air parcel along its Eulerian path into an effective behavior, which was empirically quantified by semi-conserved C_{NO_y} during the course of Lagrangian time. Although this approach was approximate, the tight relationship of concentration ratio and C_{NO_y} observed in ref (29) supported its use for the analysis herein.

The quantity $C_{O_3}(t)$ in Equation (1) was directly constrained by two observations: (1) the increase of ozone concentrations from sunrise to midafternoon (Fig. S4a) and (2) the correlation

between $C_{\rm O_3}$ and $C_{\rm NO_y}$ for afternoon time periods (Fig. S4b). Based on these observations, $C_{\rm O_3}(t)$ for an air parcel arriving at the observation site in the afternoon was empirically approximated as a function of observed $C_{\rm NO_y}$. Specifically, $C_{\rm O_3}(t)$ was represented by $C_{\rm O_3}(C_{\rm NO_y}, t)$, as explained further in the Supplementary Materials. Overall, sensitivity tests presented herein show that the influence of ozone chemistry on $C_{\rm PROD}/C_{\rm ISOP}$ and hence inferred $C_{\rm OH,noon}$ was small.

For these treatments of $C_{\text{ISOP}}(t)$, $C_{\text{OH}}(t)$, $C_{\text{O3}}(t)$, and $y_i(\text{NO})$, Equation (1) can be rewritten as follows:

$$\begin{cases}
\frac{dC_{i}}{dt} = \left[y_{i}^{*} \left(C_{\text{NO}_{y}} \right) k_{\text{ISOP,OH}} C_{\text{OH,noon}} \frac{J_{\text{O}_{3}}(t)}{J_{\text{O}_{3},\text{noon}}} + y_{i,\text{O}_{3}} k_{\text{ISOP,O}_{3}} C_{\text{O}_{3}} \left(C_{\text{NO}_{y}}, t \right) \right] C_{\text{ISOP,0}} \xi \left(1 + \frac{t}{t_{\text{ISOP}}^{*}} \right) - k_{i}(t) C_{i}(t), \quad (4) \\
C_{i}(0) = 0
\end{cases}$$

The initial concentrations of product species i are taken as zero (i.e., $C_i(0) = 0$) based on the data sets of Figure 2. The symbol ς_i , defined by $\varsigma_i = C_i/C_{\rm ISOP}$, is introduced for the product ratio. By definition, $C_{\rm PROD}/C_{\rm ISOP} = \Sigma_i \varsigma_i$. The following equation holds for $d\varsigma_i/dt$:

$$\begin{cases}
\frac{d\varsigma_{i}}{dt} = y_{i}^{*} \left(C_{\text{NO}_{y}}\right) k_{\text{ISOP,OH}} C_{\text{OH,noon}} \frac{J_{\text{O}_{3}}(t)}{J_{\text{O}_{3},\text{noon}}} + y_{i,\text{O}_{3}} k_{\text{ISOP,O}_{3}} C_{\text{O}_{3}} \left(C_{\text{NO}_{y}}, t\right) - \left(k_{i}(t) + \frac{1}{t_{\text{ISOP}}^{*} + t}\right) \varsigma_{i}(t) \\
\varsigma_{i}(0) = 0
\end{cases} \tag{5}$$

255

256

257

258

259

260

Equation (5) is derived in the Supplementary Materials. The scaling factor ξ and the initial concentration $C_{\rm ISOP,0}$ drop out. Equation (5) captures the behavior shown in Figure 3 that the ratio $C_{\rm PROD}/C_{\rm ISOP}$ is independent of isoprene emissions even as the product concentration $C_{\rm PROD}$ is not. Equation (5) also suggests that the NO_x exposure of the air mass, represented by $C_{\rm NO_y}$ here, is a key driver of $C_{\rm PROD}/C_{\rm ISOP}$ under ambient conditions through (i) effects on $y_i^*(C_{\rm NO_y})$, (ii) effects on $C_{\rm O3}(C_{\rm NO_y})$, and (iii) possible effects on $C_{\rm OH,noon}(C_{\rm NO_y})$.

The relative sensitivity of the analysis to $y_i^*(C_{NO_y})$, $C_{O_3}(C_{NO_y})$, and $C_{OH,noon}(C_{NO_y})$ is examined in Figure 4. The figure shows C_{PROD}/C_{ISOP} as a function of $C_{NO_{yy}}$ for two fixed values of $C_{\rm OH,noon}$, specifically 1×10^6 and 2×10^6 cm⁻³, using Equation (5) with and without ozone chemistry. At fixed $C_{\text{OH,noon}}$, C_{NO_y} affects $C_{\text{PROD}}/C_{\text{ISOP}}$ via the effects on $y_i^* \left(C_{\text{NO}_y} \right)$ and $C_{\rm O_3}(C_{\rm NO_y})$. Figure 4 shows that a doubling in $C_{\rm OH,noon}$ is a dominant effect on $C_{\rm PROD}/C_{\rm ISOP}$ relative to the minor effects of y_i^* and C_{O_3} . Shifts due to presence or absence of ozone chemistry are less than 10%. The simulations of Figure 4 can be compared to the observations of Figure 3c. They are in agreement that C_{PROD}/C_{ISOP} increases for greater C_{NO_y} . For fixed $C_{OH,noon}$, the relative increase is, however, smaller in the simulation than in the observations. For an increase of $C_{\rm NO}$ from 0.3 to 3.5 ppb, the simulated increase of C_{PROD}/C_{ISOP} is 50 to 60% for fixed OH concentration, whereas the observed increase is greater than 200%. Changes in y_i^* and C_{O_3} with C_{NO_v} thus do not fully explain the observed dependence of C_{PROD}/C_{ISOP} on C_{NO_y} . The implication is that changes in $C_{\text{OH,noon}}$ with $C_{\text{NO}_{\nu}}$ are important for explaining the observations. More specifically, $C_{\rm OH,noon}(C_{\rm NO,})$ can be inferred from the data set of $C_{\rm PROD}/C_{\rm ISOP}(C_{\rm NO,})$. To do so, Equation (5) was used in conjunction with the data set of $C_{PROD}/C_{ISOP}(C_{NO_y})$ plotted in Figure 3c to estimate the associated values of equivalent noontime OH concentration $C_{\rm OH,noon}$. The values are described as equivalent given the approximation of the diel variation of $C_{\mathrm{OH}}(t)$ as well as the path-averaging inherent in $y_i^* \left(C_{\mathrm{NO}_y} \right)$. For this analysis, projected values of $C_{\text{PROD}}/C_{\text{ISOP}}$ were calculated by integrating Equation (5) and summing the resultant concentration ratio ς_i of individual products for processing times of 7.5, 8.5, and 9.5 h across an array of

261

262

263

264

265

266

267

268

269

270

271

272

273

274

275

276

277

278

279

280

281

atmospherically relevant values of $C_{\text{OH,noon}}$ and C_{NO_y} . A lookup matrix of four dimensions (i.e., $C_{\text{PROD}}/C_{\text{ISOP}}$, $C_{\text{OH,noon}}$, C_{NO_y} , and t) was thereby created. A value of $C_{\text{OH,noon}}$ was obtained from the matrix based on $\{C_{\text{PROD}}/C_{\text{ISOP}}, C_{\text{NO}_y}, t\}$ for each data point of Figure 3c. The values of $C_{\text{OH,noon}}$ ranged from 0.3 to 4×10^6 cm⁻³ across the data set of Figure 3c. The quartiles were 0.8, 1.1, and 1.4×10^6 cm⁻³. The values for $C_{\text{OH,noon}}$ estimated by this analysis represent effective noontime OH concentrations that the air parcel experienced, embodying the history of oxidative capacity along its path of travel before arrival at the observation site.

Dependence of $C_{OH,noon}$ on C_{NO_v}

The retrieved $C_{\rm OH,noon}$ values are plotted versus $C_{\rm NO}_{\rm y}$ in Figure 5. The data points distribute below the 45° line of the plot, indicating that high OH concentrations occurred only for high $C_{\rm NO}_{\rm y}$. For further statistics, the $C_{\rm OH,noon}$ values were grouped by equally spaced logarithmic bins of $C_{\rm NO}_{\rm y}$, and quartile and median values were taken for each subset. The median values of $C_{\rm OH,noon}$ increased monotonically with median values of $C_{\rm NO}_{\rm y}$. For the subset of lowest $C_{\rm NO}_{\rm y}$, corresponding to a median value of 0.4 ppb, the median value of $C_{\rm OH,noon}$ was 0.6×10^6 cm⁻³. For the subset of highest $C_{\rm NO}_{\rm y}$, corresponding to a median value of 2.6 ppb, the median value of $C_{\rm OH,noon}$ was 1.5×10^6 cm⁻³. The median value of $C_{\rm OH,noon}$ thus increased by 250% for a shift in $C_{\rm NO}_{\rm y}$ from 0.4 to 2.6 ppb.

Even as there is a clear increasing trend of $C_{\text{OH,noon}}$ for increasing C_{NO_y} (Figure 5), there is also scatter in the data for high C_{NO_y} . The scatter at high C_{NO_y} could be related to some underlying approximations in the retrieval of $C_{\text{OH,noon}}$, such as the use of C_{NO_y} to represent integrated NO_x exposure. The omission from the model of possible wet deposition upwind of the observation site might also be a major factor. Although the data were screened for fair weather

locally, patchy afternoon precipitation, caused by locally induced thermal convection, frequently occurred in the study region (38). In the case that an air parcel encountered a rainfall event before arriving at the observation site, the more soluble oxidation products of isoprene might be removed preferentially relative to isoprene, and the retrieved $C_{\rm OH,noon}$ values for these cases would be biased low. The suggestion then is that the line drawn in Figure 5 is a lower estimate of the increase in $C_{\rm OH,noon}$ for increasing $C_{\rm NO}$ because of omission of wet deposition in the analysis.

Entrainment of air aloft accompanying the growth of the convective boundary layer is another important processes that can affect the inferred $C_{\text{OH,noon}}$ values. Sensitivity tests were performed to evaluate the treatment embedded in $k_i(t)$ of Equation (1) as compared to a more detailed mixing model. The results, presented in the Supplementary Materials, suggest that $C_{\text{OH,noon}}$ can be overestimated on order of 20% for higher values of C_{NO_y} , again indicating that the line drawn in Figure 5 can be an underestimate.

Random measurement errors of C_{PROD} , C_{ISOP} , and C_{NO_y} and systematic errors in the parameterizations of $C_{OH}(t)$, $C_{ISOP}(t)$, and $y_i^* \left(C_{NO_y} \right)$ were also considered. The methods are presented in the Supplementary Materials (cf. Table S2). As a result, inferred $C_{OH,noon}$ values are estimated to have a standard error of $\pm 30\%$. This uncertainty is small relative to the trend of an increase by 250% of $C_{OH,noon}$ from small to high C_{NO_y} .

In the context of the controversy involving direct OH observations (9, 19, 20), the inference of OH concentrations from measurements of isoprene and its oxidation products, as presented herein, represents an important, albeit indirect, complementary analysis. The result presented in Figure 5 serves as counterevidence to the conclusion of the earlier meta-study suggesting that OH concentrations are independent of NO_x in low- NO_x , high-isoprene environments (4). The OH concentrations obtained herein were 80% lower than those reported

using the LIF technique over rainforest in coastal eastern South America for similar isoprene concentrations. By comparison, the OH concentrations inferred by the analysis herein were comparable to concurrent GoAmazon2014/5 observations using chemical ionization mass spectrometry deployed at the same observation site (cf. Supplementary Materials). In addition, the OH concentrations fell into the range of OH concentrations inferred from previous airborne measurements over tropical forests in South America (cf. Table S3 and references therein).

In summary, the current study shows that OH concentrations inferred from measurements of isoprene and its oxidation products increased with increasing NO_y concentrations over a tropical forest in the central Amazon basin, in support of the bell-curve response represented in Figure 1. This result suggests that the oxidation capacity over tropical forests is susceptible to anthropogenic NO_x emissions. Looking into the future in Amazonia, trends of ongoing deforestation for agricultural purposes and expanding urbanization can be expected to increase demand for electricity and transport (39). Increased NO_x emissions should be expected based on current technologies. Hydroxyl radical concentrations can be expected to likewise increase, keeping other factors equal, in forested regions affected by anthropogenic pollution in Amazonia. Increased OH concentrations imply changed spatial and temporal oxidation patterns for VOCs emitted from the forest, which can have follow-on effects on visibility, cloud formation, and rainfall based on shifted mass concentration, size distribution, and chemical composition of organic particulate matter (28, 40).

Materials and Methods

Measurements were made at the "T3" site of the GoAmazon2014/5 Experiment (27). The T3 site was located in a pasture area of 2.5 km × 2 km in central Amazonia (-3.2133°, -60.5987°). Pasture regions have low emissions of isoprene (25). The site was 70 km west of Manaus, Brazil.

Steady equatorial trade winds passed over Manaus in the direction of T3. The region between the city and T3 was largely forested with interspersed agricultural activities, and the isoprene observed at T3 originated from the upwind forest. Depending on variability in the winds, the fetch of air at T3 varied from background conditions of the tropical forest (i.e., low NO_x) to polluted conditions under the influence of Manaus and regional biomass burning (i.e., higher NO_x). Measurements were made during two intensive operating periods (IOPs) that took place in the wet season (February 01 to March 31, 2014; IOP1) and in the dry season (August 15 to October 15, 2014; IOP2).

A proton-transfer-reaction time-of-flight mass spectrometer (PTR-TOF-MS, Ionicon Analytik GmbH, Austria) was employed to measure isoprene and its oxidation products (*29*). The PTR-TOF-MS was part of the Mobile Aerosol Observing System (MAOS) of the USA Department of Energy (DOE) (*27*). Isoprene (C₅H₈) was detected as the C₅H₉⁺ ion. Methyl vinyl ketone (MVK, C₄H₆O), methacrolein (MACR; C₄H₆O), and two major isoprene-derived hydroperoxide isomers (1,2)-ISOPOOH and (4,3)-ISOPOOH (C₅H₁₀O₃) were collectively detected as the C₄H₇O⁺ ion (*29*). The instrument response was calibrated using authentic standards of these compounds. The product analysis herein was based on the sum concentration of MVK, MACR, and the two ISOPOOH isomers.

Instrumentation for measuring concentrations of reactive nitrogen oxides (NO_y) was part of MAOS. The NO_y data sets were obtained from the ARM data archive (27). The operational detection limit of NO_y was 100 ppt. The NO_y concentrations were smoothed by applying a 30-min median filter to minimize the contribution of any local transient emissions, such as vehicles. Other complementary measurements at the site, such as meteorological parameters, were also obtained through the ARM data archive (27).

- 373 **Supplementary Materials** Section S1. Use of observed C_{NO_x} to represent the average NO_x exposure 374 Section S2. Determining relation $y_i^* \left(C_{NO_y} \right)$ 375 376 Section S3. Approximation of C_{O_3} 377 Section S4. Derivation of Equation (5) in the main text 378 Section S5. Additional note of Figure 4 in the main text 379 Section S6. Sensitivity tests regarding entrainment process 380 Section S7. Error analysis 381 Section S8. Comparison of $C_{OH,noon}$ obtained in this study with other OH studies 382 Fig. S1. Scatter plots of VOC concentrations with NO_v concentration for all-weather condition. Fig. S2. Simulated daily variation of photolysis frequency of ozone J_{O_3} , normalized to the 383 noontime value $J_{O_3,noon}$, based on Master Chemical Mechanism. 384 Fig. S3. Dependence on NO_y concentration of (a) ratio $y^*_{ISOPOOH}/y^*_{MVK+MACR}$ of product yield 385 386 and (**b**) product yield y^* . Fig. S4. Observation and simulation of ozone concentration C_{O_3} : (a) hourly variation and (b) 387
- Fig. S5. Simulated daytime evolution of (a) boundary layer height and (b) concentration ratio
- C_{PROD}/C_{ISOP} using a mixed boundary-layer model, which better accounts for entrainment process.
- Fig. S6. Simulated relationship of equivalent noontime OH concentration $C_{OH,noon}$ and
- concentration ratio C_{PROD}/C_{ISOP} , using the base-case model and a mixed boundary-layer model.
- Fig. S7. Variation in model parametrizations for error analysis.

correlation with NO_v concentration in afternoon hours.

- Table S1. Production yields and loss rate coefficients for isoprene oxidation products employed
- in the model.

388

Table S2. Uncertainty estimates for inferred $C_{OH,noon}$ via error propagation.

Table S3. Summary of inferred OH concentrations over tropical forests in South America

Acknowledgments

397

Institutional support was provided by the Central Office of the Large Scale Biosphere Atmosphere Experiment in Amazonia (LBA), the National Institute of Amazonian Research (INPA), and Amazonas State University (UEA). We acknowledge the Atmospheric Radiation Measurement (ARM) Climate Research Facility, a user facility of the United States Department of Energy, Office of Science, sponsored by the Office of Biological and Environmental Research, and support from the Atmospheric System Research (ASR) program of that office. We thank Dr Yi Li for helpful discussion on error analysis. The research was conducted under scientific license 001030/2012-4 of the Brazilian National Council for Scientific and Technological Development (CNPq). Funding: Funding was obtained from the United States Department of Energy (DOE; DE-SC0011115, DE-SC0011122), the Amazonas State Research Foundation (FAPEAM), and the São Paulo Research Foundation (FAPESP). Author contributions: A.B.G., A.H.G., F.N.K., P.A., R.A.F.S., K.A.M., and S.T.M. designed the research, Y.L., R.S., S.S., S.R.S., and T.B.W. performed the research, Y.L., K.A.M., and S.T.M. analyzed the data and wrote the manuscript. All the authors discussed the results, reviewed and commented the paper. Competing interests: The authors declare that they have no competing interests. Data and materials availability: All of the airborne measurement data used in the paper are available at http://www.arm.gov/campaigns/amf2014goamazon.

References

- 1. H. Levy, Normal atmosphere: large radical and formaldehyde concentrations predicted. *Science.* **173**, 141–143 (1971).
- 2. D. H. Ehhalt, Photooxidation of trace gases in the troposphere Plenary Lecture. *Phys.*

- Chem. Chem. Phys. 1, 5401–5408 (1999).
- 3. L. C. Valin, A. R. Russell, R. C. Cohen, Variations of OH radical in an urban plume inferred from NO₂ column measurements. *Geophys. Res. Lett.* **40**, 1856–1860 (2013).
- 4. F. Rohrer, K. Lu, A. Hofzumahaus, B. Bohn, T. Brauers, C.-C. Chang, H. Fuchs, R. Haseler, F. Holland, M. Hu, K. Kita, Y. Kondo, X. Li, S. Lou, A. Oebel, M. Shao, L. Zeng, T. Zhu, Y. Zhang, A. Wahner, Maximum efficiency in the hydroxyl-radical-based self-cleansing of the troposphere. *Nat. Geosci.* 7, 559–563 (2014).
- 5. J. Lelieveld, T. M. Butler, J. N. Crowley, T. J. Dillon, H. Fischer, L. Ganzeveld, H. Harder, M. G. Lawrence, M. Martinez, D. Taraborrelli, J. Williams, Atmospheric oxidation capacity sustained by a tropical forest. *Nature*. **452**, 737–40 (2008).
- 6. L. K. Whalley, P. M. Edwards, K. L. Furneaux, A. Goddard, T. Ingham, M. J. Evans, D. Stone, J. R. Hopkins, C. E. Jones, A. Karunaharan, J. D. Lee, A. C. Lewis, P. S. Monks, S. J. Moller, D. E. Heard, Quantifying the magnitude of a missing hydroxyl radical source in a tropical rainforest. *Atmos. Chem. Phys.* 11, 7223–7233 (2011).
- 7. A. Hofzumahaus, F. Rohrer, K. D. Lu, B. Bohn, T. Brauers, C. C. Chang, H. Fuchs, F. Holland, K. Kita, Y. Kondo, X. Li, S. R. Lou, M. Shao, L. M. Zeng, A. Wahner, Y. H. Zhang, Amplified trace gas removal in the troposphere. *Science*. **324**, 1702–1704 (2009).
- 8. D. Tan, I. Faloona, J. B. Simpas, W. Brune, P. B. Shepson, T. L. Couch, a. L. Sumner, M. a. Carroll, T. Thornberry, E. Apel, D. Riemer, W. Stockwell, HO_x budgets in a deciduous forest: Results from the PROPHET summer 1998 campaign. *J. Geophys. Res. Atmos.* **106**, 24407–24427 (2001).
- 9. J. Mao, X. Ren, L. Zhang, D. M. Van Duin, R. C. Cohen, J. H. Park, A. H. Goldstein, F. Paulot, M. R. Beaver, J. D. Crounse, P. O. Wennberg, J. P. DiGangi, S. B. Henry, F. N. Keutsch, C. Park, G. W. Schade, G. M. Wolfe, J. A. Thornton, W. H. Brune, Insights into hydroxyl measurements and atmospheric oxidation in a California forest. *Atmos. Chem. Phys.* 12, 8009–8020 (2012).
- 10. S. Dusanter, D. Vimal, P. S. Stevens, R. Volkamer, L. T. Molina, A. Baker, S. Meinardi, D. Blake, P. Sheehy, A. Merten, R. Zhang, J. Zheng, E. C. Fortner, W. Junkermann, M. Dubey, T. Rahn, B. Eichinger, P. Lewandowski, J. Prueger, H. Holder, Measurements of OH and HO₂ concentrations during the MCMA-2006 field campaign Part 2: Model comparison and radical budget. *Atmos. Chem. Phys.* 9, 6655–6675 (2009).
- 11. Y. Kanaya, R. Cao, H. Akimoto, M. Fukuda, Y. Komazaki, Y. Yokouchi, M. Koike, H. Tanimoto, N. Takegawa, Y. Kondo, Urban photochemistry in central Tokyo: 1. Observed and modeled OH and HO₂ radical concentrations during the winter and summer of 2004. *J. Geophys. Res. Atmos.* **112**, D21312 (2007).
- 12. X. R. Ren, H. Harder, M. Martinez, R. L. Lesher, A. Oliger, J. B. Simpas, W. H. Brune, J. J. Schwab, K. L. Demerjian, Y. He, X. L. Zhou, H. G. Gao, OH and HO₂ chemistry in the urban atmosphere of New York City. *Atmos. Environ.* **37**, 3639–3651 (2003).
- 13. K. D. Lu, A. Hofzumahaus, F. Holland, B. Bohn, T. Brauers, H. Fuchs, M. Hu, R. Häseler, K. Kita, Y. Kondo, X. Li, S. R. Lou, A. Oebel, M. Shao, L. M. Zeng, A. Wahner, T. Zhu, Y. H. Zhang, F. Rohrer, Missing OH source in a suburban environment near Beijing: observed and modelled OH and HO₂ concentrations in summer 2006. *Atmos. Chem. Phys.* **13**, 1057–1080 (2013).
- 14. T. J. Dillon, J. N. Crowley, Direct detection of OH formation in the reactions of HO₂ with CH₃C(O)O₂ and other substituted peroxy radicals. *Atmos. Chem. Phys.* **8**, 4877–4889 (2008).

- 15. H. Fuchs, A. Hofzumahaus, F. Rohrer, B. Bohn, T. Brauers, H. P. Dorn, R. Haseler, F. Holland, M. Kaminski, X. Li, K. Lu, S. Nehr, R. Tillmann, R. Wegener, A. Wahner, Experimental evidence for efficient hydroxyl radical regeneration in isoprene oxidation. *Nat. Geosci.* **6**, 1023–1026 (2013).
- 16. J. Peeters, T. L. Nguyen, L. Vereecken, HO_x radical regeneration in the oxidation of isoprene. *Phys. Chem. Chem. Phys.* **11**, 5935–5939 (2009).
- 17. Y. J. Liu, I. Herdlinger-Blatt, K. A. McKinney, S. T. Martin, Production of methyl vinyl ketone and methacrolein via the hydroperoxyl pathway of isoprene oxidation. *Atmos. Chem. Phys.* **13**, 5715–5730 (2013).
- 18. J. D. Crounse, F. Paulot, H. G. Kjaergaard, P. O. Wennberg, Peroxy radical isomerization in the oxidation of isoprene. *Phys. Chem. Chem. Phys.* **13**, 13607–13613 (2011).
- 19. P. A. Feiner, W. H. Brune, D. O. Miller, L. Zhang, R. C. Cohen, P. S. Romer, A. H. Goldstein, F. N. Keutsch, K. M. Skog, P. O. Wennberg, T. B. Nguyen, A. P. Teng, J. DeGouw, A. Koss, R. J. Wild, S. S. Brown, A. Guenther, E. Edgerton, K. Baumann, J. L. Fry, Testing atmospheric oxidation in an Alabama forest. *J. Atmos. Sci.* **73**, 4699–4710 (2016).
- 20. A. Novelli, K. Hens, C. Tatum Ernest, D. Kubistin, E. Regelin, T. Elste, C. Plass-Dülmer, M. Martinez, J. Lelieveld, H. Harder, Characterisation of an inlet pre-injector laser-induced fluorescence instrument for the measurement of atmospheric hydroxyl radicals. *Atmos. Meas. Tech.* 7, 3413–3430 (2014).
- C. A. Stroud, J. M. Roberts, P. D. Goldan, W. C. Kuster, P. C. Murphy, E. J. Williams, D. Hereid, D. Parrish, D. Sueper, M. Trainer, F. C. Fehsenfeld, E. C. Apel, D. Riemer, B. Wert, B. Henry, A. Fried, M. Martinez-Harder, H. Harder, W. H. Brune, G. Li, H. Xie, V. L. Young, Isoprene and its oxidation products, methacrolein and methylvinyl ketone, at an urban forested site during the 1999 Southern Oxidants Study. *J. Geophys. Res.* 106, 8035–8046 (2001).
- U. Kuhn, M. O. Andreae, C. Ammann, A. C. Araújo, E. Brancaleoni, P. Ciccioli, T. Dindorf, M. Frattoni, L. V Gatti, L. Ganzeveld, B. Kruijt, J. Lelieveld, J. Lloyd, F. X. Meixner, A. D. Nobre, U. Pöschl, C. Spirig, P. Stefani, A. Thielmann, R. Valentini, J. Kesselmeier, Isoprene and monoterpene fluxes from Central Amazonian rainforest inferred from tower-based and airborne measurements, and implications on the atmospheric chemistry and the local carbon budget. *Atmos. Chem. Phys.* 7, 2855–2879 (2007).
- 23. T. Karl, A. Guenther, R. J. Yokelson, J. Greenberg, M. Potosnak, D. R. Blake, P. Artaxo, The tropical forest and fire emissions experiment: Emission, chemistry, and transport of biogenic volatile organic compounds in the lower atmosphere over Amazonia. *J. Geophys. Res. Atmos.* **112**, D18302 (2007).
- 24. R. G. Prinn, R. F. Weiss, B. R. Miller, J. Huang, F. N. Alyea, D. M. Cunnold, P. J. Fraser, D. E. Hartley, P. G. Simmonds, Atmospheric trends and lifetime of CH₃CCI₃ and global OH concentrations. *Science.* **269**, 187–192 (1995).
- 25. A. Guenther, X. Jiang, C. L. Heald, T. Sakulyanontvittaya, T. Duhl, L. K. Emmons, X. Wang, The Model of Emissions of Gases and Aerosols from Nature version 2.1 (MEGAN2.1): an extended and updated framework for modeling biogenic emissions. *Geosci. Model Dev.* 5, 1471–1492 (2012).
- 26. R. Atkinson, J. Arey, Gas-phase tropospheric chemistry of biogenic volatile organic compounds: a review. *Atmos. Environ.* **37**, S197–S219 (2003).

- 27. S. T. Martin, P. Artaxo, L. A. T. Machado, A. O. Manzi, R. A. F. Souza, C. Schumacher, J. Wang, M. O. Andreae, H. M. J. Barbosa, J. Fan, G. Fisch, A. H. Goldstein, A. Guenther, J. L. Jimenez, U. Pöschl, M. A. Silva Dias, J. N. Smith, M. Wendisch, Introduction: Observations and modeling of the Green Ocean Amazon (GoAmazon2014/5). *Atmos. Chem. Phys.* 16, 4785–4797 (2016).
- S. T. Martin, P. Artaxo, L. Machado, A. O. Manzi, R. A. F. Souza, C. Schumacher, J. Wang, T. Biscaro, J. Brito, A. Calheiros, K. Jardine, A. Medeiros, B. Portela, S. S. de Sá, K. Adachi, A. C. Aiken, R. Albrecht, L. Alexander, M. O. Andreae, H. M. J. Barbosa, M. Wendisch, et al., The Green Ocean Amazon experiment (GoAmazon2014/5) observes pollution affecting gases, aerosols, clouds, and rainfall over the rain forest. Bull. Am. Meteorol. Soc. 98, 981–997 (2016).
- 29. Y. Liu, J. Brito, M. R. Dorris, J. C. Rivera-Rios, R. Seco, K. H. Bates, P. Artaxo, S. Duvoisin, F. N. Keutsch, S. Kim, A. H. Goldstein, A. B. Guenther, A. O. Manzi, R. A. F. Souza, S. R. Springston, T. B. Watson, K. A. McKinney, S. T. Martin, Isoprene photochemistry over the Amazon rainforest. *Proc. Natl. Acad. Sci. U. S. A.* 113, 6125–6130 (2016).
- 30. M. E. Jenkin, J. C. Young, A. R. Rickard, The MCM v3.3.1 degradation scheme for isoprene. *Atmos. Chem. Phys.* **15**, 11433–11459 (2015).
- 31. S. S. de Sá, B. B. Palm, P. Campuzano-Jost, D. A. Day, M. K. Newburn, W. Hu, G. Isaacman-VanWertz, L. D. Yee, R. Thalman, J. Brito, S. Carbone, P. Artaxo, A. H. Goldstein, A. O. Manzi, R. A. F. Souza, F. Mei, J. E. Shilling, S. R. Springston, J. Wang, J. D. Surratt, M. L. Alexander, J. L. Jimenez, S. T. Martin, Influence of urban pollution on the production of organic particulate matter from isoprene epoxydiols in central Amazonia. *Atmos. Chem. Phys.* 17, 6611–6629 (2017).
- 32. P. S. Bakwin, S. C. Wofsy, S.-M. Fan, Measurements of reactive nitrogen oxides (NO_y) within and above a tropical forest canopy in the wet season. *J. Geophys. Res. Atmos.* **95**, 16765–16772 (1990).
- 33. P. Ploton, R. Pelissier, C. Proisy, T. Flavenot, N. Barbier, S. N. Rai, P. Couteron, Assessing aboveground tropical forest biomass using Google Earth canopy images. *Ecol. Appl.* **22**, 993–1003 (2012).
- D. Gu, A. B. Guenther, J. E. Shilling, H. Yu, M. Huang, C. Zhao, Q. Yang, S. T. Martin, P. Artaxo, S. Kim, R. Seco, T. Stavrakou, K. M. Longo, J. Tóta, R. A. F. de Souza, O. Vega, Y. Liu, M. Shrivastava, E. G. Alves, F. C. Santos, G. Leng, Z. Hu, Airborne observations reveal elevational gradient in tropical forest isoprene emissions. *Nat. Commun.* 8, 15541 (2017).
- 35. A. Monin, The structure of atmospheric turbulence. *Theory Probab. Appl.* **3**, 266–296 (1958).
- 36. A. J. Huisman, J. R. Hottle, M. M. Galloway, J. P. DiGangi, K. L. Coens, W. Choi, I. C. Faloona, J. B. Gilman, W. C. Kuster, J. de Gouw, N. C. Bouvier-Brown, A. H. Goldstein, B. W. LaFranchi, R. C. Cohen, G. M. Wolfe, J. A. Thornton, K. S. Docherty, D. K. Farmer, M. J. Cubison, J. L. Jimenez, J. Mao, W. H. Brune, F. N. Keutsch, Photochemical modeling of glyoxal at a rural site: observations and analysis from BEARPEX 2007. *Atmos. Chem. Phys.* 11, 8883–8897 (2011).
- 37. F. Rohrer, H. Berresheim, Strong correlation between levels of tropospheric hydroxyl radicals and solar ultraviolet radiation. *Nature*. **442**, 184–187 (2006).
- 38. A. K. Betts, J. D. Fuentes, M. Garstang, J. H. Ball, Surface diurnal cycle and boundary

- layer structure over Rondônia during the rainy season. J. Geophys. Res. Atmos. 107, 8065 (2002).
- 39. E. A. Davidson, A. C. de Araujo, P. Artaxo, J. K. Balch, I. F. Brown, M. M. C. Bustamante, M. T. Coe, R. S. DeFries, M. Keller, M. Longo, J. W. Munger, W. Schroeder, B. S. Soares-Filho, C. M. Souza, S. C. Wofsy, The Amazon basin in transition. *Nature*. **481**, 321–328 (2012).
- 40. U. Pöschl, S. T. Martin, B. Sinha, Q. Chen, S. S. Gunthe, J. A. Huffman, S. Borrmann, D. K. Farmer, R. M. Garland, G. Helas, J. L. Jimenez, S. M. King, A. Manzi, E. Mikhailov, T. Pauliquevis, M. D. Petters, A. J. Prenni, P. Roldin, D. Rose, J. Schneider, H. Su, S. R. Zorn, P. Artaxo, M. O. Andreae, Rainforest aerosols as biogenic nuclei of clouds and precipitation in the Amazon. *Science*. 329, 1513–1516 (2010).
- 41. M. Trainer, D. D. Parrish, M. P. Buhr, R. B. Norton, F. C. Fehsenfeld, K. G. Anlauf, J. W. Bottenheim, Y. Z. Tang, H. A. Wiebe, J. M. Roberts, R. L. Tanner, L. Newman, V. C. Bowersox, J. F. Meagher, K. J. Olszyna, M. O. Rodgers, T. Wang, H. Berresheim, K. L. Demerjian, U. K. Roychowdhury, Correlation of ozone with NO_y in photochemically aged air. *J. Geophys. Res. Atmos.* **98**, 2917–2925 (1993).
- 42. J. Vilà-Guerau de Arellano, E. G. Patton, T. Karl, K. van den Dries, M. C. Barth, J. J. Orlando, The role of boundary layer dynamics on the diurnal evolution of isoprene and the hydroxyl radical over tropical forests. *J. Geophys. Res. Atmos.* **116**, D07304 (2011).
- 43. J. Vilà-Guerau de Arellano, K. van den Dries, D. Pino, On inferring isoprene emission surface flux from atmospheric boundary layer concentration measurements. *Atmos. Chem. Phys.* **9**, 3629–3640 (2009).
- 44. S. Kim, G. M. Wolfe, L. Mauldin, C. Cantrell, A. Guenther, T. Karl, A. Turnipseed, J. Greenberg, S. R. Hall, K. Ullmann, E. Apel, R. Hornbrook, Y. Kajii, Y. Nakashima, F. N. Keutsch, J. P. DiGangi, S. B. Henry, L. Kaser, R. Schnitzhofer, M. Graus, A. Hansel, W. Zheng, F. F. Flocke, Evaluation of HO_x sources and cycling using measurement-constrained model calculations in a 2-methyl-3-butene-2-ol (MBO) and monoterpene (MT) dominated ecosystem. *Atmos. Chem. Phys.* 13, 2031–2044 (2013).
- 45. D. J. Jacob, S. C. Wofsy, Budgets of reactive nitrogen, hydrocarbons, and ozone over the Amazon forest during the wet season. *J. Geophys. Res. Atmos.* **95**, 16737–16754 (1990).
- 46. C. Warneke, R. Holzinger, A. Hansel, A. Jordan, W. Lindinger, U. Poschl, J. Williams, P. Hoor, H. Fischer, P. J. Crutzen, H. A. Scheeren, J. Lelieveld, Isoprene and its oxidation products methyl vinyl ketone, methacrolein, and isoprene related peroxides measured online over the tropical rain forest of Surinam in March 1998. *J. Atmos. Chem.* **38**, 167–185 (2001).
- 47. J. Williams, U. Poschl, P. J. Crutzen, A. Hansel, R. Holzinger, C. Warneke, W. Lindinger, J. Lelieveld, An atmospheric chemistry interpretation of mass scans obtained from a proton transfer mass spectrometer flown over the tropical rainforest of Surinam. *J. Atmos. Chem.* **38**, 133–166 (2001).
- 48. R. Atkinson, D. L. Baulch, R. A. Cox, J. N. Crowley, R. F. Hampson, R. G. Hynes, M. E. Jenkin, M. J. Rossi, J. Troe, Evaluated kinetic and photochemical data for atmospheric chemistry: Volume II gas phase reactions of organic species. *Atmos. Chem. Phys.* **6**, 3625–4055 (2006).
- 49. J. M. St. Clair, J. C. Rivera-Rios, J. D. Crounse, H. C. Knap, K. H. Bates, A. P. Teng, S. Jørgensen, H. G. Kjaergaard, F. N. Keutsch, P. O. Wennberg, Kinetics and products of the reaction of the first-generation isoprene hydroxy hydroperoxide (ISOPOOH) with OH. *J.*

- Phys. Chem. A. 120, 1441–1451 (2016).
- 50. T. B. Nguyen, J. D. Crounse, A. P. Teng, J. M. St. Clair, F. Paulot, G. M. Wolfe, P. O. Wennberg, Rapid deposition of oxidized biogenic compounds to a temperate forest. *Proc. Natl. Acad. Sci. U. S. A.* **112**, E392–E401 (2015).

Figures

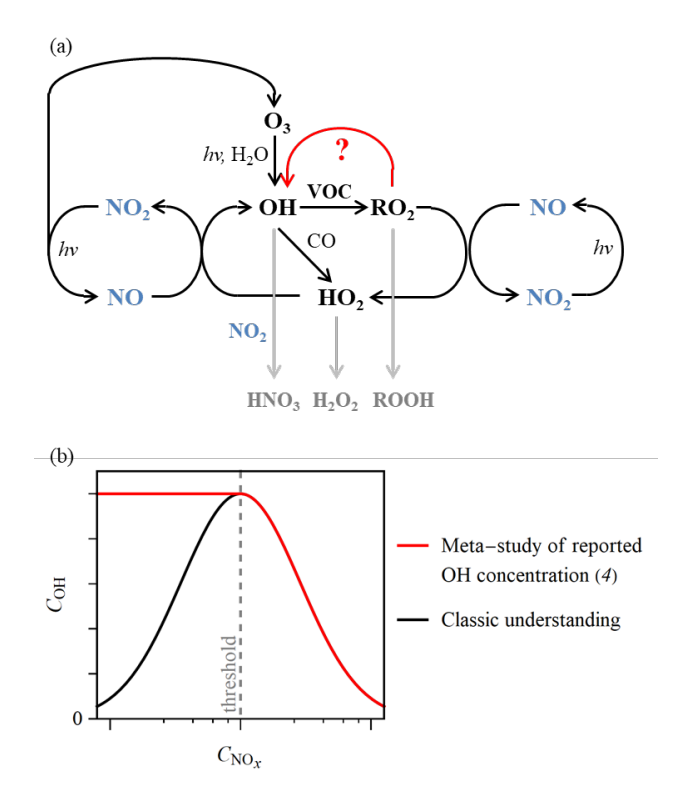


Figure 1. (a) Illustration of the chemical cycles connecting OH production and loss to NO_x and VOC species. (b)

Illustration of the dependence of OH concentration on NO_x concentration. The classical dependence of the bell curve in black can be compared to the absence of a dependence (i.e., the red horizontal line) below a threshold NO_x concentration, as suggested by the meta-study of Rohrer et al. (4).

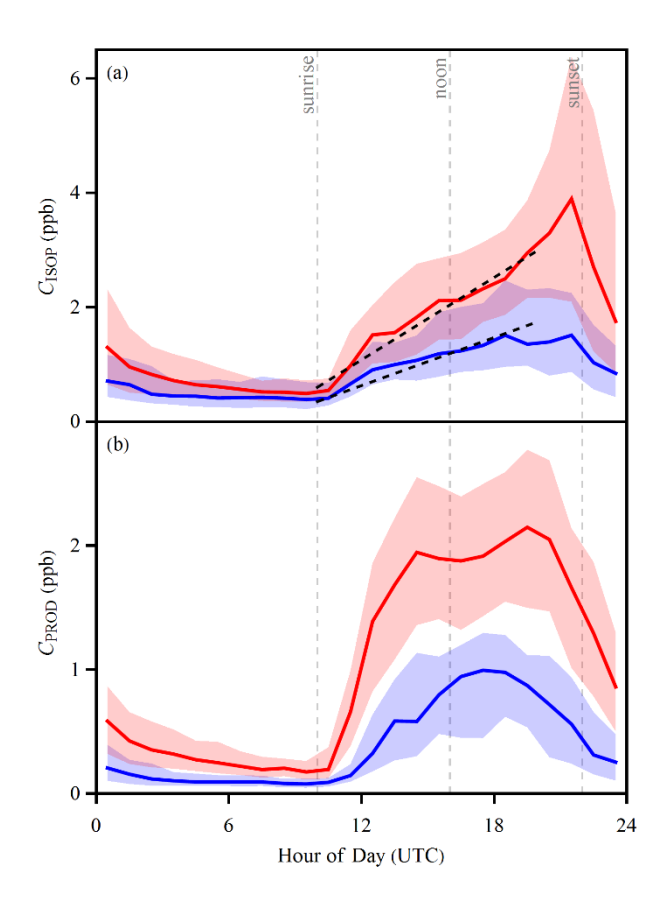


Figure 2. Hourly variation of (a) isoprene concentration C_{ISOP} and (b) product concentration C_{PROD} . The vertical dashed gray lines demarcate local sunrise, noon, and sunset (UTC less 4 h). Data are shown in the wet and dry seasons in blue and red colors, respectively. The solid line and shaded regions respectively represent the median and interquartile ranges of the data sets for each hour of the day. The two black dashed lines in panel (a) show the simulated increase of C_{ISOP} from sunrise to midafternoon using Equation (2) for $C_{ISOP,0}$ values of 0.35 and 0.6 ppb.

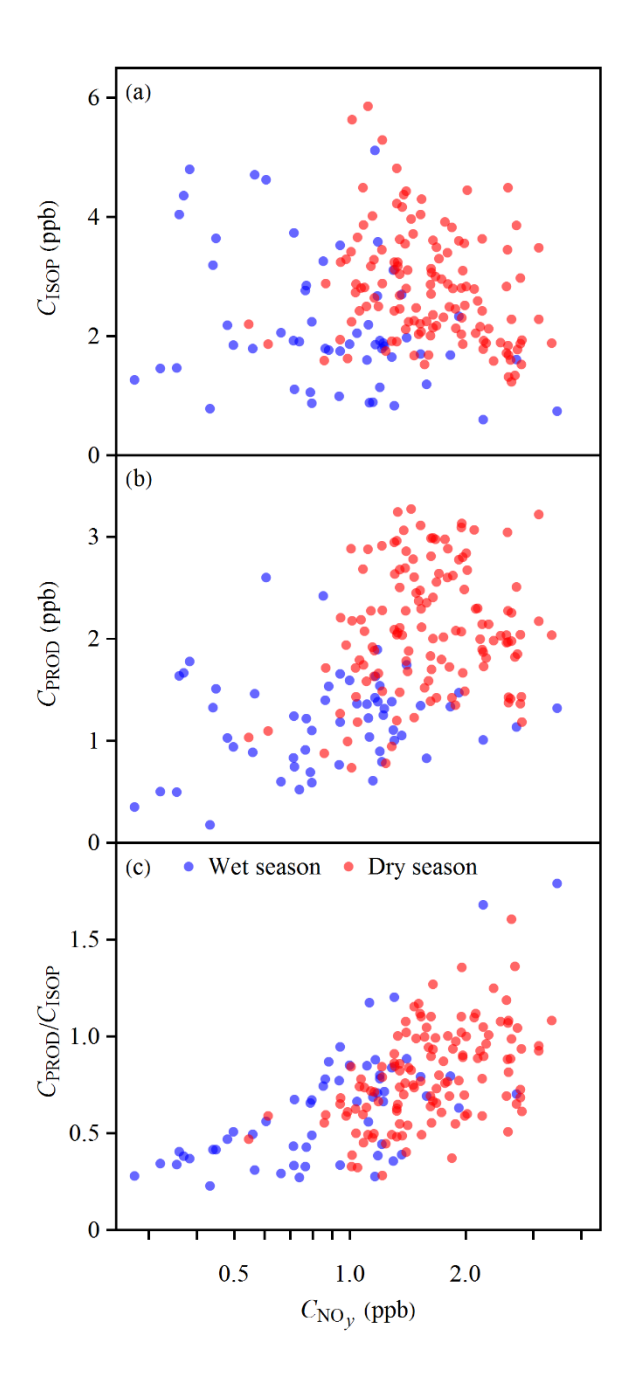


Figure 3. Scatter plots of VOC concentrations with NO_y concentration. (a) Isoprene concentration C_{ISOP} . (b) Sum concentration C_{PROD} of isoprene oxidation products. (c) Concentration ratio C_{PROD}/C_{ISOP} . Data points represent hourly averages recorded within a time window of 13:00 to 16:00 (local time) (17:00 to 20:00 UTC). Blue and red points correspond to the wet and dry seasons, respectively, for fair-weather conditions. All-weather data, including periods of heavy rainfall or prolonged overcast conditions, are presented in Supplementary Figure S1.

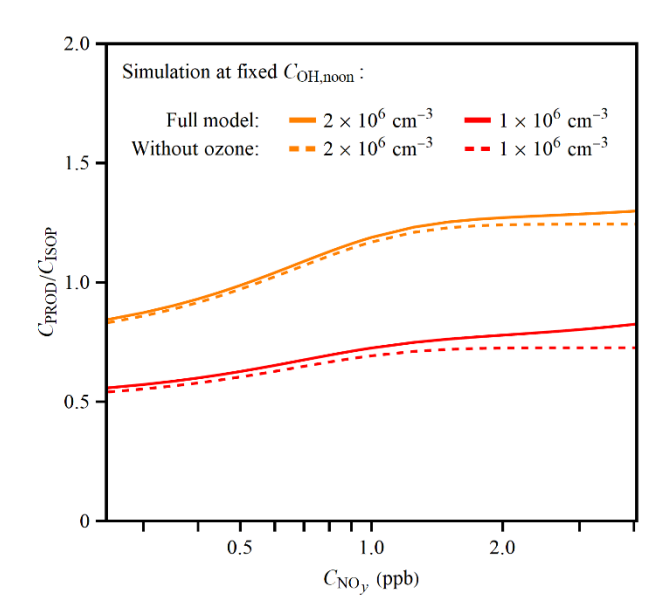


Figure 4. Simulated dependence of the concentration ratio $C_{\text{PROD}}/C_{\text{ISOP}}$ on NO_y concentration C_{NO_y} . Results are shown for two different values of $C_{\text{OH,noon}}$ as well as the full model compared to a model that omitted isoprene ozonolysis. At fixed $C_{\text{OH,noon}}$, C_{NO_y} affects $C_{\text{PROD}}/C_{\text{ISOP}}$ via the effects on $y_i^*\left(C_{\text{NO}_y}\right)$ and $C_{\text{O_3}}(C_{\text{NO}_y})$ (cf. Equation (5)). Solid lines show results for the full model of Equation (5), and dashed lines show results for a model that omits isoprene ozonolysis (i.e., $C_{\text{O_3}} = 0$). For all cases, t = 8.5 h, corresponding to 14:30 (local time).

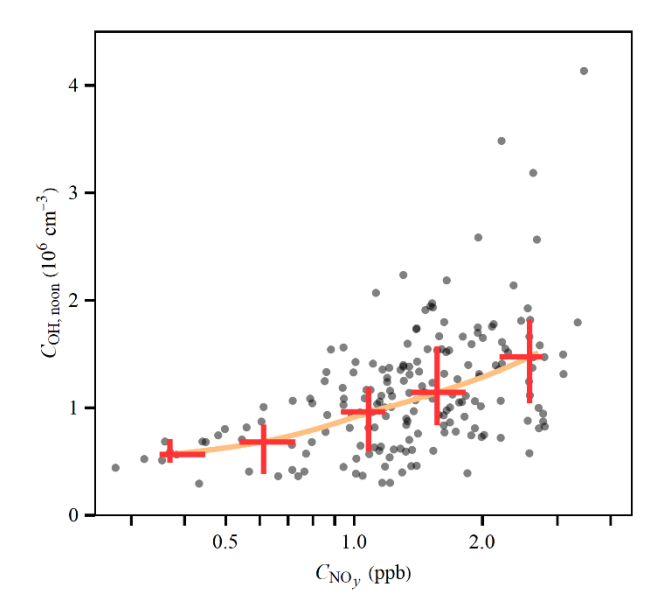


Figure 5. Dependence of inferred equivalent noontime OH concentration $C_{\text{OH,noon}}$ on NO_y concentration. The gray dots represent $C_{\text{OH,noon}}$ inferred for the individual data points of Figure 3c. The red crosses represent medians and quartiles after grouping the data points into five equally spaced bins based on logarithmic NO_y concentrations. The orange line connects the medians of the binned data.

Supplementary Materials

Full Title

Isoprene photo-oxidation products quantify the effect of pollution on hydroxyl radicals over Amazonia

Short Title

Effect of pollution on OH radicals

Authors

Yingjun Liu, ¹† Roger Seco, ² Saewung Kim, ² Alex B. Guenther, ² Allen H. Goldstein, ³ Frank N. Keutsch, ^{1,4} Stephen R. Springston, ⁵ Thomas B. Watson, ⁵ Paulo Artaxo, ⁶ Rodrigo A. F. Souza, ⁷ Karena A. McKinney, ¹‡* and Scot T. Martin ^{1,8}*

Affiliations

- ¹ School of Engineering and Applied Sciences, Harvard University, Cambridge, Massachusetts, United States
- ² Department of Earth System Science, University of California, Irvine, California, United States.
- ³ Department of Environmental Science, Policy and Management, University of California, Berkeley, California, United States.
- ⁴ Department of Chemistry and Chemical Biology, Harvard University, Cambridge, Massachusetts, United States.
- ⁵ Department of Environmental and Climate Sciences, Brookhaven National Laboratory, Upton, New York, United States.
- ⁶ Department of Applied Physics, University of São Paulo, São Paulo, Brazil.
- ⁷ Department of Meteorology, Amazonas State University, Manaus, Amazonia, Brazil.
- ⁸ Department of Earth and Planetary Sciences, Harvard University, Cambridge, Massachusetts, United States.
- † Now at Department of Environmental Science, Policy and Management, University of California, Berkeley, California, United States
- ‡ Now at Department of Chemistry, Colby College, Waterville, Maine, United States
- * To whom correspondence should be addressed. E-mail: scot_martin@harvard.edu, kamckinney@seas.harvard.edu

Journal

Science Advances

- 1 **Section S1.** Use of observed C_{NO_y} to represent the average NO_x exposure
- The observed NO_y concentration C_{NO_y} was used to quantify NO_x exposure of an air parcel
- passing over T3 site, which had affected the observed C_{PROD}/C_{ISOP} . The major NO_x sources for
- 4 air masses passing over T3 site included background emissions from forests, regional biomass
- 5 burning, and anthropogenic emissions in the city of Manaus. Emissions from forests and regional
- 6 biomass burning were diffusive NO_x sources. If these emissions dominated, the use of observed
- 7 C_{NO_x} to represent the average NO_x exposure of the air parcel is a reasonable assumption. Manaus,
- 8 located 4 to 6 h upwind of T3 site, was a point source of NO_x . Observed C_{NO_y} at T3 site can
- 9 indicate NO_x exposure of the air parcel after passing over Manaus, but may not reflect the NO_x
- 10 exposure before that. Nevertheless, the 4 to 6 h from Manaus in mid-morning to T3 site in mid-
- afternoon was the most intense period of isoprene photooxidation during a day, i.e., high
- isoprene concentration (Figure 2a) and high OH concentration (Figure S2). That is, NO_x
- 13 concentrations during that period had a dominant influence on the ratio C_{PROD}/C_{ISOP} observed at
- 14 T3. The use of C_{NO_y} to represent NO_x exposure can be problematic in extreme cases when
- observed NO_{ν} was primarily emitted in the vicinity of the observation site instead of far upwind,
- 16 for instance from nearby biomass burning. This scenario occurred occasionally, indicative by
- elevated ratio of C_{NO}/C_{NO_v} or C_{NO_v}/C_{NO_v} . For the data presented in Figure 3c, no nearby biomass
- burning event was, however, clearly identified by the ratios.

- 19 **Section S2.** Determining relation $y_i^* (C_{NO_y})$
- Relation $y_i^*(C_{NO_y})$ was determined based on observations and analysis presented in ref (29) for
- 21 the same observation site. Ref (29) showed that the concentration ratio $C_{\rm ISOPOOH}/C_{\rm MVK+MACR}$
- correlated tightly with $C_{NO_{\nu}}$ and that the concentration ratio can be transformed to the effective
- production ratio $y^*_{\text{ISOPOOH}}/y^*_{\text{MVK+MACR}}$ by combining the measurements with kinetic modeling. In
- 24 Ref (29), only $C_{\rm ISOPOOH}/C_{\rm MVK+MACR}$ under background condition was transformed to
- 25 $y_{\text{ISOPOOH}}/y_{\text{MVK+MACR}}$. In the current study, the same transformation was applied to all the data
- points in the plot of $C_{\text{ISOPOOH}}/C_{\text{MVK+MACR}}$ versus C_{NO_y} in Ref (29), so that a plot of
- 27 $y_{\text{ISOPOOH}}^*/y_{\text{MVK+MACR}}^*$ versus C_{NO_y} can be obtained. A fit of the plot led to the following empirical
- 28 relation of $y^*_{ISOPOOH}/y^*_{MVK+MACR}$ and C_{NO_y} :

$$y_{\text{ISOPOOH}}^* / y_{\text{MVK+MACR}}^* = 3.8 \text{ Exp}(-3.4 C_{\text{NO}_v}), \tag{S1}$$

- 30 which is presented in Figure S3a. The empirical relation $y^*_{\text{ISOPOOH}}/y^*_{\text{MVK+MACR}}(C_{\text{NO}_{V}})$ in Equation
- 31 (S1) was then used to derive $y_i^* (C_{NO_y})$ based on two approximations. First, $y_{ISOPOOH}$ +
- 32 $y_{\text{MVK+MACR}}$ was 0.7 across the observed NO_y range (29, 30). Secondly, $y_{(1,2)\text{-ISOPOOH}}/y_{(4.3)\text{-ISOPOOH}}$
- had the same value as $y_{\text{MVK}}/y_{\text{MACR}}$ determined in laboratory experiments (17). The obtained
- relations $y_i^*(C_{NO_y})$, where *i* is one of MVK, MACR, (1,2)-ISOPOOH, and (4,3)-ISOPOOH, were
- 35 shown in Figure S3b.

- 36 **Section S3.** Approximation of C_{O_3}
- 37 The observed diel variation of ozone concentrations C_{O_3} (Fig. S4a) and correlation of afternoon
- values of C_{O_3} and C_{NO_v} (Fig. S4b) was used to constrain C_{O_3} as a function of t and C_{NO_v} . As
- 39 shown in Fig. S4a, C_{O_3} started to increase after sunrise and peaked in midafternoon. The
- 40 observed time dependence before 16:00 local time was represented empirically by the following
- 41 equation:

42
$$C_{O_3}(t) = C_{O_3}^* \left(1 - \exp\left[-\frac{t}{12000}\right] \right),$$
 (S2)

- 43 where $C_{O_3}^*$ was a daily scaling factor representing the variability in ozone concentrations for
- each day, and t was the time since sunrise in seconds. Values of $C_{O_3}^*$ of 15 and 40 ppb in
- Equation S2 were used to approximate the time dependence of median C_{O_3} in the wet and dry
- seasons, respectively (Fig. S4a). As shown in Fig. S4b, C_{O_3} and C_{NO_y} correlated in afternoon
- 47 hours, as often observed for photochemically aged air (41). Considering an average reaction time
- of 8.5 h in the afternoon, the linear fit of C_{O_3} and C_{NO_v} in Fig. S4b allowed for approximating the
- 49 dependence of $C_{O_3}^*$ on C_{NO_y} :

54

$$C_{O_3}^* = \frac{C_{O_3,afternoon}}{1 - \text{Exp}[-\frac{8.5 \times 3600}{12000}]} = \frac{6.4 + 18C_{NO_y}}{0.92}.$$
 (S3)

- 51 Combining Eqns. (S2) and (S3), the daily course of ozone concentration can be approximated as
- 52 a function of afternoon concentration C_{NO_y} as follow:

53
$$C_{O_3}(C_{NO_y}, t) = \frac{6.4 + 18C_{NO_y}}{0.92} \left(1 - \exp\left[-\frac{t}{12000}\right] \right).$$
 (S4)

- 55 **Section S4.** Derivation of Equation (5) in the main text
- For products species i of isoprene oxidation, where i is one of (1,2)-ISOPOOH, (4,3)-ISOPOOH,
- 57 MVK, or MACR, the time course of product concentrations $C_i(t)$ in an air mass is governed by
- 58 the following family of equations (i.e., Equation (1) in the main text):

59
$$\frac{dC_i}{dt} = y_i(\text{NO}) k_{\text{ISOP,OH}} C_{\text{OH}}(t) C_{\text{ISOP}}(t) + y_{i,O_3} k_{\text{ISOP,O}_3} C_{O_3}(t) C_{\text{ISOP}}(t) - k_i(t) C_i(t), \quad (S5)$$

- where y_i is the production yield of product species i from the reaction between hydroxy radical
- and isoprene, and it varies according to the fate of ISOPOO, which is largely controlled by the
- NO concentration and hence susceptible to pollution; $C_{OH}(t)$, $C_{ISOP}(t)$, and $C_{O_3}(t)$ are the
- concentrations of hydroxyl radical, isoprene, and ozone, respectively, which vary strongly with
- 64 time of day; $k_{\rm ISOP,OH}$ and $k_{\rm ISOP,O3}$ are the reaction rate constant of isoprene with hydroxyl radical
- and ozone, respectively; y_{i,O_3} is the production yield of product speicies i from the reaction
- between ozone and isoprene; and k_i is a composite, pseudo-first order loss coefficient of species
- 67 i, given by $k_i(t) = k_{i,OH} C_{OH}(t) + k_{i,O_3} C_{O_3}(t) + k_{i,en} + k_{i,de}$ for bimolecular reaction between species
- 68 i and the hydroxyl radical (OH), atmospheric entrainment (en), and surface deposition (de).
- Supplementary Table S1 present typical values of y_{i,O_3} , $k_{i,OH}$, k_{i,O_3} , $k_{i,en}$, and $k_{i,de}$ for central
- 70 Amazonia, partly reproduced from Liu et al. (29).
- The time course of ratio $\varsigma_i(t)$ of concentration of products species i to isoprene
- 72 concentration is governed by the following equation:

73
$$\frac{dS_i}{dt} = \frac{d(C_i / C_{ISOP})}{dt} = \frac{1}{C_{ISOP}(t)} \frac{dC_i}{dt} - \frac{C_i(t)}{C_{ISOP}^2(t)} \frac{dC_{ISOP}}{dt}.$$
 (S6)

74 Taking Equation (S5) into Equation (S6), we have

75
$$\frac{d\varsigma_{i}}{dt} = y_{i}(\text{NO}) k_{\text{ISOP,OH}} C_{\text{OH}}(t) + y_{i,O_{3}} k_{\text{ISOP,O_{3}}} C_{O_{3}}(t) - k_{i}(t) \frac{C_{i}(t)}{C_{\text{ISOP}}(t)} - \frac{C_{i}(t)}{C_{\text{ISOP}}^{2}(t)} \frac{dC_{\text{ISOP}}}{dt}$$

$$= y_{i}(\text{NO}) k_{\text{ISOP,OH}} C_{\text{OH}}(t) + y_{i,O_{3}} k_{\text{ISOP,O_{3}}} C_{O_{3}}(t) - (k_{i}(t) + \frac{1}{C_{\text{ISOP}}(t)} \frac{dC_{\text{ISOP}}}{dt}) \varsigma_{i}(t)$$
(S7)

- The term $C_{\rm ISOP}(t)$ is empirically represented by the following linear equation (i.e.,
- 77 Equation (2) in the main text):

78
$$C_{\text{ISOP}}(t) = \xi C_{\text{ISOP},0} \left(1 + t/t_{\text{ISOP}}^* \right),$$
 (S8)

- where ξ was a daily scaling factor representing the variability in isoprene concentrations for each
- 80 day, $C_{\text{ISOP},0}$ was the typical isoprene concentration at time zero (sunrise), and t_{ISOP}^* was the
- 81 typical characteristic time for C_{ISOP} to double its initial value. Taking Equation (S8) into
- 82 Equation (S7), we have

83
$$\frac{d\varsigma_{i}}{dt} = y_{i}(\text{NO}) k_{\text{ISOP,OH}} C_{\text{OH}}(t) + y_{i,O_{3}} k_{\text{ISOP,O}_{3}} C_{O_{3}}(t) - (k_{i}(t) + \frac{1}{\xi C_{\text{ISOP,0}}} (1 + t/t_{\text{ISOP}}^{*}) \frac{\xi C_{\text{ISOP,0}}}{t_{\text{ISOP}}^{*}}) \varsigma_{i}(t)$$

$$= y_{i}(\text{NO}) k_{\text{ISOP,OH}} C_{\text{OH}}(t) + y_{i,O_{3}} k_{\text{ISOP,O}_{3}} C_{O_{3}}(t) - (k_{i}(t) + \frac{1}{t + t_{\text{ISOP}}^{*}}) \varsigma_{i}(t)$$
(S9)

- where quantities ξ and $C_{\rm ISOP,0}$ are dropped off in the analysis. Further replacing $y_i(NO)$ in
- Equation (S9) with $y_i^* (C_{NO_y})$, replacing $C_{O_3}(t)$ with $C_{O_3}(C_{NO_y}, t)$ (Equation (S4)), and assuming
- 86 $C_{\text{OH}}(t) = C_{\text{OH,noon}} \frac{J_{O_3}(t)}{J_{O_{3,\text{noon}}}}$ (Equation (3) in the main text), we have:

87
$$\frac{d\varsigma_{i}}{dt} = y_{i}^{*} \left(C_{\text{NO}_{y}} \right) k_{\text{ISOP,OH}} C_{\text{OH,noon}} \frac{J_{\text{O}_{3}}(t)}{J_{\text{O}_{3},\text{noon}}} + y_{i,\text{O}_{3}} k_{\text{ISOP,O}_{3}} C_{\text{O}_{3}} \left(C_{\text{NO}_{y}}, t \right) - \left(k_{i}(t) + \frac{1}{t_{\text{ISOP}}^{*} + t} \right) \varsigma_{i}(t), \quad (S10)$$

- which constitutes Equation (5) in the main text.
- Equation (Error! Reference source not found.5) is a first-order linear differential
- 90 equation, and its general analytical solution is given by

91
$$\varsigma_i(t) = \frac{1}{e^{\int P(t)dt}} \int e^{\int P(t)dt} Q(t)dt, \qquad (S11)$$

92 where

93
$$P(t) = k_{i}(t) + \frac{1}{t_{\text{ISOP}}^{*} + t}$$

$$Q(t) = y_{i}^{*} \left(C_{\text{NO}_{y}}\right) k_{\text{ISOP,OH}} C_{\text{OH,noon}} \frac{J_{\text{O}_{3}}(t)}{J_{\text{O}_{3},\text{noon}}} + y_{i,\text{O}_{3}} k_{\text{ISOP,O}_{3}} C_{\text{O}_{3}}(C_{\text{NO}_{y}}, t)$$

- Equation (S11) contains complex integral terms, which cannot be done analytically. Equation
- 95 (Error! Reference source not found.5) was thus integrated numerically in the current analysis.

- 96 **Section S5.** Additional note of Figure 4 in the main text
- The simulated increase of C_{PROD}/C_{ISOP} with increasing C_{NO_y} at zero ozone (dashed lines in Figure
- 98 4) arises from the different lifetimes of MVK, MACR, (1,2)-ISOPOOH, and (4,3)-ISOPOOH.
- 99 For reference, these four products have respective lifetimes against OH reaction of 14 h, 10 h, 4
- 100 h, and 2 h for $C_{\rm OH} = 1 \times 10^6$ cm⁻³ (cf. Table S1 and references therein). The lifetimes of the
- 101 ISOPOOH isomers, which are the dominant products for low NO concentrations, are about 70%
- shorter than those of MVK and MACR. As a consequence, the concentration ratio of C_{PROD}/C_{ISOP}
- is lower at lower C_{NO_y} , all other factors being equal. The ratio levels off at high C_{NO_y} once MVK
- and MACR become the dominant products.

Section S6. Sensitivity tests regarding entrainment process

Entrainment of air masses aloft associated with the growth of the convective boundary layer can influence C_{PROD}/C_{ISOP} and C_{NO_y} . Treatment of entrainment process in the model thus affects the inferred C_{OH} . In our base-case model, the entrainment process is considered but in a simplified way (cf. note in Table S1). This simplification is evaluated through a series of sensitivity tests using a mixed boundary-layer model (MXL), which couples chemistry with boundary layer dynamics and allows for explicit modeling of the entrainment processes (42, 43).

In the MXL approach, the evolution of the boundary layer height h is explicitly simulated, driven by the surface heat fluxes that are prescribed to the model. The entrainment velocity v_{en} is taken as the growth rate of the boundary layer height (dh/dt). The concentration discontinuity between the mixed layer and the inversion layer/free troposphere is represented by a zero-order jump. The approach assumes that under convective conditions strong turbulent mixing causes perfect mixing of quantities over the entire depth of the boundary layer. Arellano $et\ al.\ (43)$ showed that the concentration profiles of isoprene simulated using MXL for Amazon condition were comparable to the profiles simulated using the Large-Eddy Simulation technique coupled to a chemistry module. For the MXL model, the counterpart of Equation (5) in the main text is given by

$$\frac{d\varsigma_{i}}{dt} = y_{i}^{*} \left(C_{\text{NO}_{y}}\right) k_{\text{ISOP,OH}} C_{\text{OH,noon}} \frac{J_{\text{O}_{3}}(t)}{J_{\text{O}_{3},\text{noon}}} + y_{i,\text{O}_{3}} k_{\text{ISOP,O}_{3}} C_{\text{O}_{3}}(C_{\text{NO}_{y}}, t) \\
- \left(k_{i,\text{OH}} C_{\text{OH,noon}} \frac{J_{\text{O}_{3}}(t)}{J_{\text{O}_{3},\text{noon}}} + k_{i,\text{O}_{3}} C_{\text{O}_{3}}(C_{\text{NO}_{y}}, t) + \frac{v_{de,i}}{h(t)} + \frac{1}{h(t)} \frac{dh}{dt} + \frac{1}{t_{\text{ISOP}}^{*} + t} \right) \varsigma_{i}(t) + \frac{1}{h(t)} \frac{dh}{dt} \frac{C_{i,\text{upper}}(h, t)}{C_{\text{ISOP}}(t)} \tag{S12}$$

To use Equation (S12), we have to know the isoprene concentration $C_{ISOP}(t)$ in the mixed layer as well as the product concentration $C_{i,upper}(h, t)$ above the boundary layer. In the real atmosphere, $C_{i,upper}$ is expected to be a function of time and height, yet there is little observational constraint of the dependence. In the sensitivity analysis below, $C_{i,upper}$ is assumed across a range

of values, bounded by an upper limit equivalent to typical product concentration around sunset when the mixed layer collapses (i.e., no nocturnal dilution of residual products in the inversion layer) and a lower limit of 0 ppb (i.e., residual products from previous day fully removed by dilution or wet deposition). Figure S5 presents an example of simulation results using this approach. The model was run under typical conditions in the wet season. The simulated evolution of boundary layer height is in good agreement with retrievals from the discrete radiosonde measurements at the site (Figure S5a). The simulated evolution of C_{PROD}/C_{ISOP} is shown in Fig. S5b for $C_{PROD,upper}$ ranging from 0 to 0.6 ppb. The value of 0.6 ppb is a typical product concentration in the boundary layer before sunset during the wet season (cf. Fig 2 in the main text). As shown in Fig. S5b, C_{PROD}/C_{ISOP} is higher for higher $C_{PROD,upper}$, yet the difference decreases with time of the day. In the morning when the boundary layer is shallow and fast-growing, entrainment from air aloft has a large impact on C_{PROD}/C_{ISOP} . The value of C_{PROD}/C_{ISOP} simulated using the upper limit of $C_{\text{PROD upper}}$ is up to 5 times higher than that simulated using the lower limit. Later in the day, growth of the boundary layer slows and photochemistry speeds up, each of which lessens the impact of entrainment on C_{PROD}/C_{ISOP} . The difference in simulated C_{PROD}/C_{ISOP} of the two limiting cases diminishes to 30% in afternoon hours. In the current study, the OH retrieval is based on C_{PROD}/C_{ISOP} in the afternoon hours, when C_{PROD}/C_{ISOP} was less sensitive to the entrainment processes. Figure S6 displays retrieved $C_{OH,noon}$ for given C_{PROD}/C_{ISOP} at 18.5 UTC (14.5 local time), determined using the base-case model and the MXL model, respectively. Model parameters were kept the same as the simulation in Figure S5. The MXL simulations with $C_{PROD,upper}$ of 0 and 0.6 ppb provides upper and lower bounds for retrieved $C_{\rm OH,noon}$, respectively, and the band width is

127

128

129

130

131

132

133

134

135

136

137

138

139

140

141

142

143

144

145

146

147

148

149

150	up to 0.7×10^6 cm ⁻³ . The $C_{\rm OH,noon}$ retrieved using the base-case model generally falls into the
151	range suggested by the MXL model, close to the lower limit at upper C_{PROD}/C_{ISOP} and vice versa
152	For high C_{PROD}/C_{ISOP} , $C_{OH,noon}$ retrieved using the base-case model can be an underestimate by
153	up to 20%. The level of agreement between the MXL and base-case model simulation indicates
154	that parameterization of entrainment in the base-case model is a reasonable simplification. The
155	potential bias associated with the simplification (i.e., underestimating $C_{\mathrm{OH,noon}}$ at higher
156	C_{PROD}/C_{ISOP} and overestimating at lower C_{PROD}/C_{ISOP}) indicates the line drawn in Fig. 5 ($C_{OH,noon}$)
157	versus $C_{\text{NO}_{y}}$) in the main text can be an underestimate, given that higher $C_{\text{PROD}}/C_{\text{ISOP}}$ was
158	observed at higher C_{NO_y} (Fig. 3c in the main text).

159 **Section S7.** Error analysis

- Uncertainties in inferred $C_{\rm OH,noon}$ can arise from uncertainties in measurements, uncertainties in model parameterization, and assumptions in the inference (forward) model. The uncertainties associated with measurements and model parameterization are evaluated using a numeric error propagation approach described below.
- The current work tackles an inverse problem, which is to infer $C_{\text{OH,noon}}$ for given C_{NO_y} and $C_{\text{PROD}}/C_{\text{ISOP}}$ at a specific time point t, based on a forward model:

166
$$C_{PROD}/C_{ISOP}(t) = F(C_{NO_y}, C_{OH,noon}, t, p_1, p_2...p_n),$$
 (S13)

- where function F can be obtained from Equation (S11) and $p_1, p_2...p_n$ represent various
- modeling parameters. Assuming that G is the inverse of function F, defined as

$$C_{\text{OH,noon}} = G(C_{\text{PROD}}/C_{\text{ISOP}}, C_{\text{NO}_{\text{v}}}, t, p_1, p_2...p_n), \tag{S14}$$

- the standard deviation $S_{COH noon}$ of retrieved $C_{OH,noon}$ can be estimated by error propagation via
- function G as follows:

$$S_{C_{\text{OH,noon}}} = \sqrt{\sum \left(\frac{\partial G}{\partial x}\right)^2 S_x^2}; \ x \in \{C_{\text{Prod}}/C_{\text{ISOP}}, C_{\text{NO}_y}, p_1, p_1 L \ p_n\},$$
 (S15)

- where S_x is the standard deviation of observable/parameter x. Equation (S15) is based on linear
- characteristics of the gradient of G. Specifically, a linear approximation of G has to be valid
- inside a neighborhood of radius S_x . Equation (S15) also neglects the correlation of variables.
- Based on Eq. (S15), the key of uncertainty estimation through error propagation is to
- determine $\partial G/\partial x$ for any observable/parameter x. Since Equation (S11) and hence the function F
- 178 contain complex integral terms, the inverse function G cannot be obtained analytically. Instead
- we took an alternative numeric approach to derive $\partial G/\partial x$ for any given $\{C_{PROD}/C_{ISOP}', C_{NO_v}', t'\}$.
- 180 It involves four steps:

181	(1) numerically solving Eq. (S11) at $\{C_{NO_y}', t'\}$ and a range of prescribed $C_{OH,noon}$ values to
182	get a list of $\{C_{PROD}/C_{ISOP}, C_{OH,noon}\}$ pairs;
183	(2) interpolating the $\{C_{PROD}/C_{ISOP}, C_{OH,noon}\}$ pairs to determine the corresponding $C_{OH,noon}$
184	for given C_{PROD}/C_{ISOP} ';
185	(3) varying parameter x in the forward model around the central value x_0 and redoing steps
186	(1-2) to generate a list of $\{x, C_{OH,noon'}\}$ pairs; and
187	(4) interpolating the $\{x, C_{OH,noon}'\}$ pairs and taking the derivative at $x = x_0$, which is the value
188	of $\partial G/\partial x(x_{\theta})$.
189	The numerical approach outlined above determines the value of $\partial G/\partial x$ locally at a specific point
190	$\{C_{PROD}/C_{ISOP}', C_{NO_y}', t'\}$ and thereby estimates the local uncertainty of $C_{OH,noon}$. In addition, the
191	numerical simulation (x versus $C_{OH,noon}$) also helps to validate the major underlying assumption
192	of Eq. (S15), i.e., a linear approximation of G inside a neighborhood of radius S_x .
193	Table S2 presents the results of uncertainty estimates for three cases. The uncertainty
194	analysis considers random errors of observables C_{PROD}/C_{ISOP} and C_{NO_y} as well as systematic
195	errors of three modeling parameters t^*_{ISOP} , $p_{NO_{y,yield}}$ and $p_{OH,t}$. They are respectively associated to
196	three approximations quantitatively most important in the retrieval of $C_{\text{OH,noon}}$, including $C_{\text{ISOP}}(t)$,
197	$y_i^*(C_{NO_y})$, and $C_{OH}(t)$. Lognormal error distribution is assumed for each of the three modeling
198	parameters. Table S2 presents the best-estimate standard error S associated to each observable or
199	parameter. The resultant variation of $C_{\text{ISOP}}(t)$, $y_i^* \left(C_{\text{NO}_y}\right)$, and $C_{\text{OH}}(t)$ due to standard variation of
200	t_{ISOP}^* , $p_{\text{NO}_{y},\text{yield}}$ and $p_{\text{OH,t}}$ is presented in Fig. S7 (a-c), respectively.
201	The relative standard error $S_{COH,noon}$ of inferred $C_{OH,noon}$ ranged from 23% to 30% for the
202	three cases in Table S2, which represent data points at the three corners of the triangle-shape

203	scatter plot of C_{PROD}/C_{ISOP} versus C_{NO_y} (Fig. 3c in the main text). This level of uncertainty in
204	inferred $C_{\text{OH,noon}}$ values would not affect the derived dependence of $C_{\text{OH,noon}}$ on C_{NO_y} . The largest
205	contribution of $S_{C_{\rm OH,noon}}$ is from errors of observable $C_{\rm PROD}/C_{\rm ISOP}$, followed by systematic errors
206	of parameters $p_{OH,t}$ (i.e., time dependence of C_{OH}) and t^*_{ISOP} . Errors in NO _y related terms,
207	including C_{NO_y} or $p_{NO_y,yield}$, have smaller contribution, in particular at higher C_{NO_y} .

208 **Section S8.** Comparison of $C_{OH,noon}$ obtained in this study with other studies

The OH values obtained in the current study can be compared with several other studies.

- (1) LIF measurement over rainforest in South America (5)
- 211 Aircraft measurements over rainforests on the east coast of South America reported daytime OH
- concentration of $(5.6 \pm 1.9) \times 10^6$ cm⁻³ for background condition (5). Laser-Induced-Florescence
- 213 (LIF) technique was used for the OH measurement. By comparison, the equivalent noontime OH
- 214 concentration for background central Amazon conditions derived in the current study is $(6.8 \pm$
- 2.1) × 10^5 cm⁻³ (Figure 5), which is less than 15% of daytime OH value reported in Ref (5). The
- study in Ref (5) was, however, 1500 km northeast of the present study in a coastal region, so
- 217 factors other than possible measurement discrepancies could lead to a difference in OH
- 218 concentrations in the two regions.

210

230

- (2) Concurrent CIMS measurement at the same observation site
- 220 During GoAmazon 2014/5 campaign, OH concentrations were monitored at the same site of
- current study using Chemical Ionization Mass Spectrometry (CIMS) (44). The CIMS
- measurements suggested an average midday maximum OH concentration of 1.2×10^6 cm⁻³ in the
- wet season (sparse data in the dry season). By comparison, the inter-quartile range of $C_{\rm OH,noon}$
- derived using the current method was $(0.5-1.2) \times 10^6$ cm⁻³ for the wet season, with a standard
- error of $\pm 30\%$. The statistics of inferred $C_{\text{OH,noon}}$ characterize the regional oxidation capacity over
- 226 the Amazon basin upwind of the observation site, since the air parcels arriving at the site can
- have varied backward trajectories. By comparison, the OH concentrations measured by CIMS
- were instantaneous values specific to the observation site. Keeping these differences in the mind,
- 229 the inferred OH values are consistent with the CIMS observations.
 - (3) Inferred OH concentration over rainforests in South America

Table S2 summarizes OH concentrations inferred from VOC observations over rainforests in South America. The earlier studies were based on airborne measurements in the wet seasons (45–47). The OH concentrations were simulated using observation-constrained box model with simplified chemical mechanism. Simulated daytime maximum OH concentrations were in the range of $(0.6\text{-}1.5) \times 10^6$ cm⁻³, which is consistent with the inferred $C_{\text{OH,noon}}$ in this study for the wet season, with an inter-quartile range of $(0.5\text{-}1.2) \times 10^6$ cm⁻³. The more recent OH estimates were based on airborne measurements in the dry seasons (22, 23). The OH concentration were inferred using two methods: (1) vertical gradient of concentration ratio $C_{\text{PROD}}/C_{\text{ISOP}}$ in the boundary layer and (2) budget of biogenic VOCs in the boundary layer. The estimated daytime OH concentration ranged from $(1.3 \pm 0.5) \times 10^6$ cm⁻³ to $(3\text{-}8) \times 10^6$ cm⁻³. In this study, the interquartile range of inferred $C_{\text{OH,noon}}$ for the dry season was $(0.8\text{-}1.5) \times 10^6$, which fell into the lower range of previous estimates.

Supplementary Figures

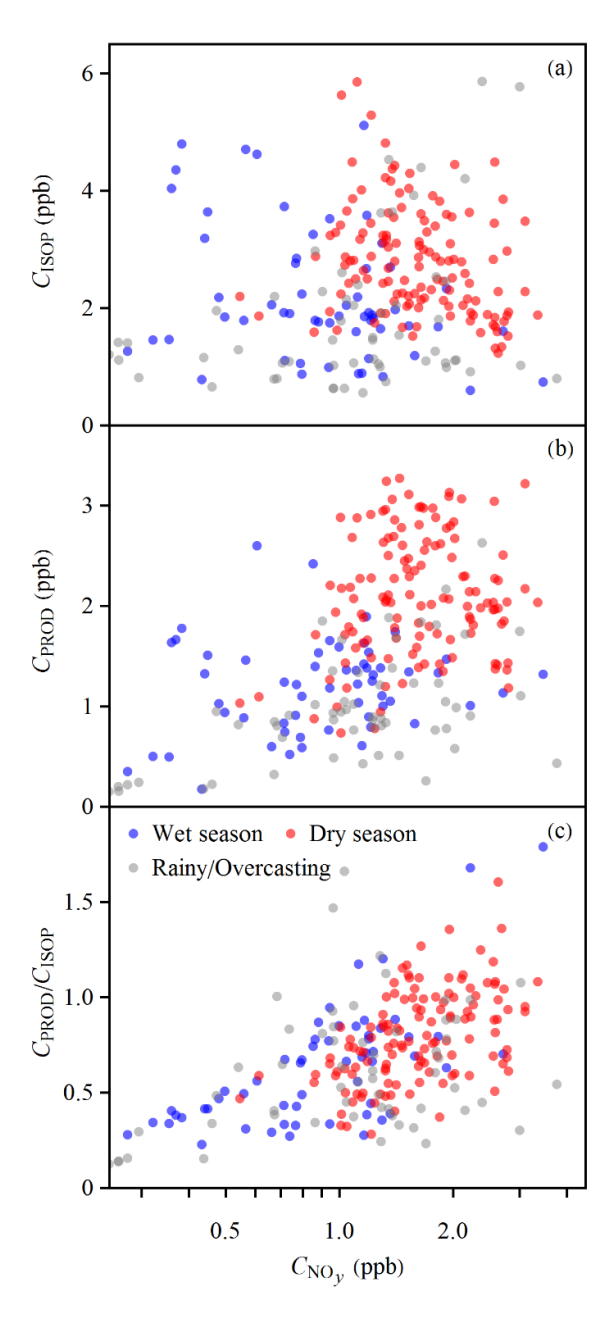


Figure S1. Scatter plots of VOC concentrations with NO_y concentration for all-weather condition. (a) Isoprene concentration $C_{\rm ISOP}$. (b) Sum concentration $C_{\rm PROD}$ of isoprene oxidation products. (c) Concentration ratio $C_{\rm PROD}/C_{\rm ISOP}$. Data points represent hourly averages from 17:00 - 20:00 UTC (13:00 - 16:00 local time). Data are shown for the wet and dry seasons in blue and red colors, respectively, for fairweather conditions. There are 57 data points for the wet season and 128 for the dry season. The gray points, representing data recorded in either season at times of heavy rainfall or overcast conditions, are not included in the analysis.

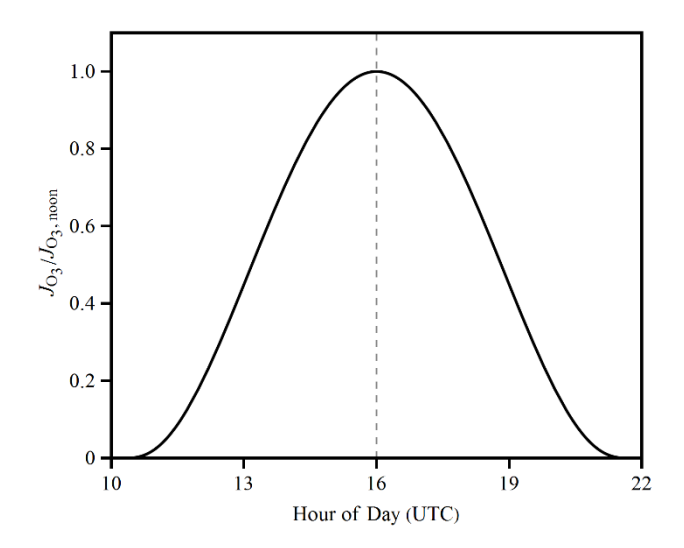


Figure S2. Simulated daily variation of photolysis frequency of ozone J_{O_3} , normalized to the noontime value $J_{O_3,noon}$, based on Master Chemical Mechanism (30). The dashed line represents local noon.

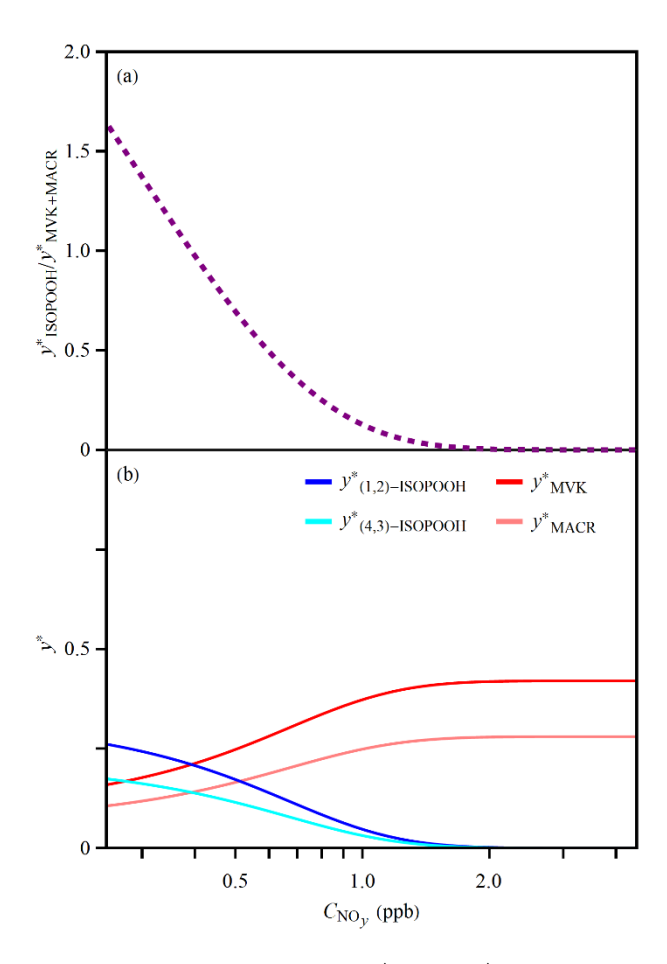


Figure S3. Dependence on NO_y concentration of (a) ratio $y^*_{\text{ISOPOOH}}/y^*_{\text{MVK+MACR}}$ of product yield and (b) product yield y^* . The presented result is based on observations and analysis presented in ref (29). See also Section S2 in the Supplementary Materials.

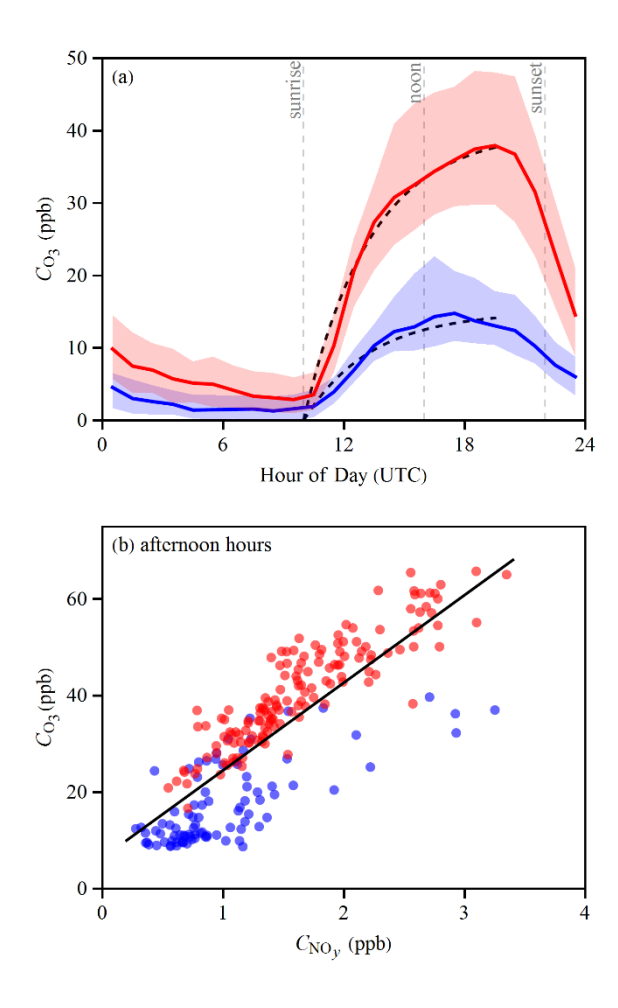


Figure S4. Observation and simulation of ozone concentration $C_{\rm O_3}$: (a) hourly variation and (b) correlation with NO_y concentration in afternoon hours. Data are shown in the wet and dry seasons in blue and red colors, respectively. For panel (a), the solid line and shaded regions respectively represent the median and interquartile ranges of the data sets for each hour of the day. The two black dashed lines show the simulated increase of $C_{\rm O_3}$ from sunrise to midafternoon using Equation (S2) for $C_{\rm O_3}^*$ values of 15 and 40 ppb. The vertical dashed gray lines demarcate local sunrise, noon, and sunset (UTC less 4 h). For panel (b): hourly concentrations within a time window of 13:00-16:00 (local time) were shown, for fair-weather conditions (the same as Figure 3 in the main text). The black line represent linear fit of observed $C_{\rm O_3}$ and $C_{\rm NO_y}$.

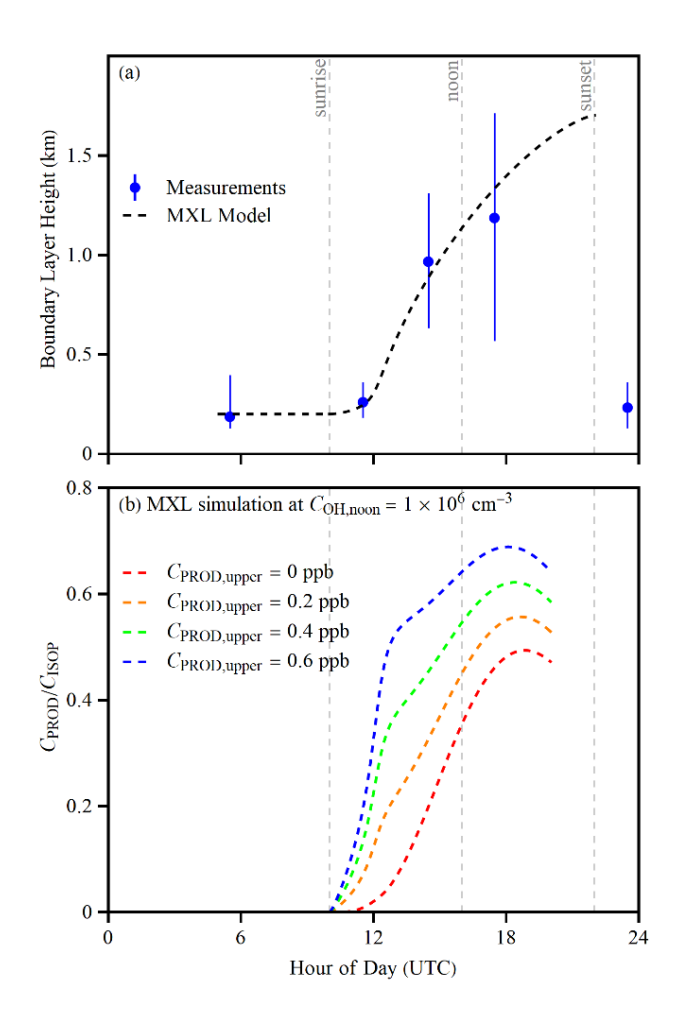


Figure S5. Simulated daytime evolution of (a) boundary layer height and (b) concentration ratio C_{PROD}/C_{ISOP} using a mixed boundary layer (MXL) model, which better accounts for entrainment process. Details of MXL model are presented in Section S6 of the Supplementary Materials. The simulation is run under typical condition of the wet season ($y_{MVK+MACR} = y_{ISOPOOHs} = 0.35$; $C_{O_3} = 12$ ppb, $C_{ISOP,0} = 0.35$ ppb). The noontime OH concentration $C_{OH,noon}$ is set as 1.0×10^6 cm⁻³. In panel (a), blue dot and line represent median and inter-quartile range of boundary layer height retrieved from radiosonde measurements in the wet season. In panel (b), simulation results are shown for $C_{PROD,upper}$ of 0, 0.2, 0.4, and 0.6 ppb.

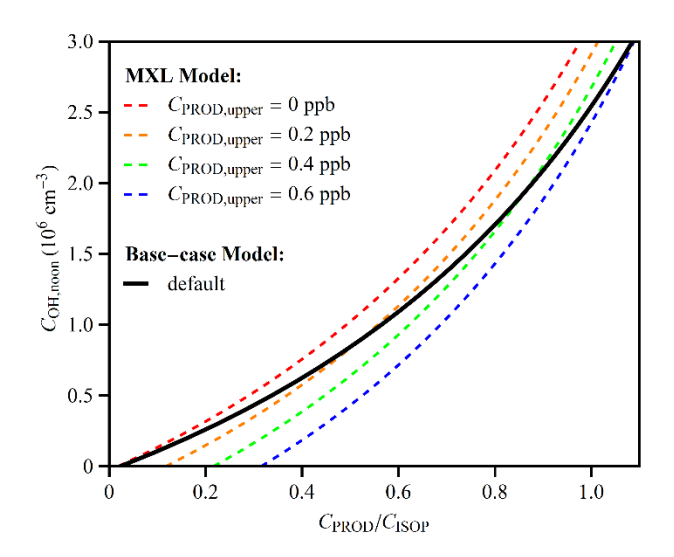


Figure S6. Simulated relationship of equivalent noontime OH concentration $C_{\rm OH,noon}$ and concentration ratio $C_{\rm PROD}/C_{\rm ISOP}$, using the base-case model and a MXL model. Details of the MXL model are presented in Section S6 of the Supplementary Materials. The simulation is run under typical condition of the wet season $(y_{\rm MVK+MACR} = y_{\rm ISOPOOHs} = 0.35; C_{\rm O_3} = 12 \text{ ppb}, C_{\rm ISOP,0} = 0.35 \text{ ppb}, t = 8.5 \text{ h})$. For MXL modeling, simulation results are shown for $C_{\rm PROD,upper}$ of 0, 0.2, 0.4, and 0.6 ppb.

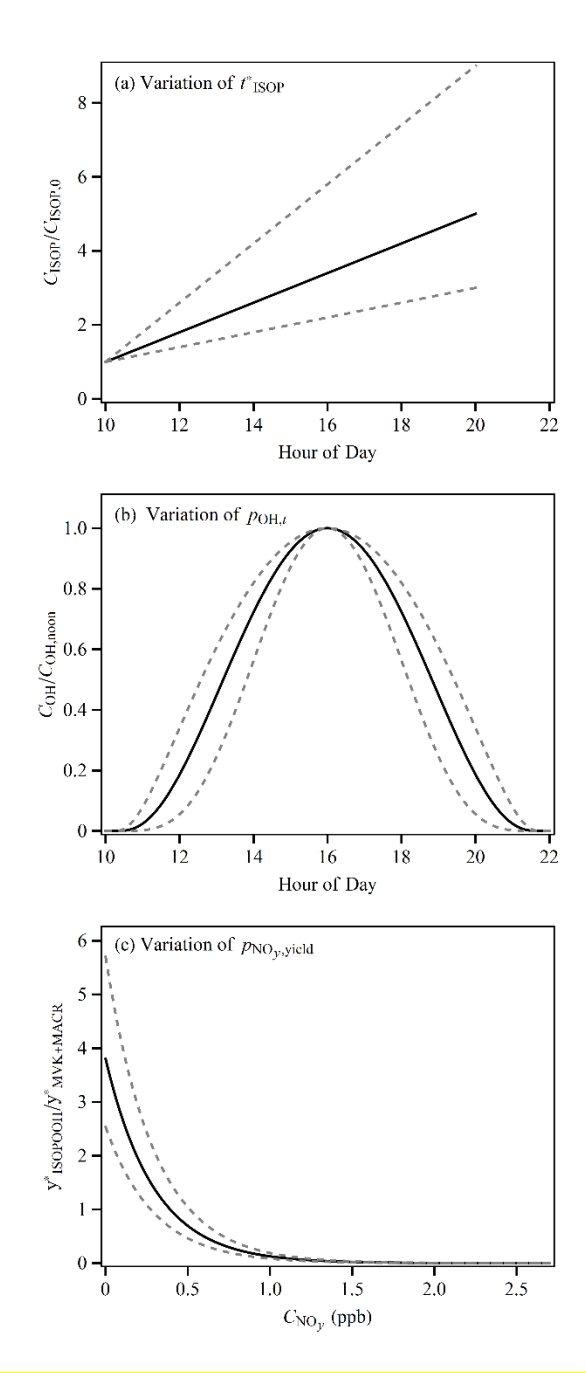


Figure S7. Variation in model parametrizations for error analysis. Panels (**a**), (**b**), (**c**) present parametrizations for $C_{\text{ISOP}}(t)$, $C_{\text{OH}}(t)$, and $y_i^* \left(C_{\text{NO}_y} \right)$, respectively. The black line represents best-estimate parameterization. The grey dashed lines represent parameterizations using best-estimate value +/- standard error of associated modeling parameters (cf. Table S2).

Supplementary Tables

Table S1. Production yields and loss rate coefficients for isoprene oxidation products employed in the model. This table is partly reproduced from Liu et al. (29). A 1000-m deep, well mixed planetary boundary layer (PBL) is assumed. A temperature of 298 K is used.

Species,i	<i>y</i> _{i,O3} *	$\frac{k_{i,\text{OH}}^{\dagger}}{(10^{-11} \text{ cm}^3 \text{ s}^{-1})}$	k_{i,O_3}^{\dagger} (10 ⁻¹⁸ cm ³ s ⁻¹)	$k_{i,de}^{\ddagger}$ (10 ⁻⁵ s ⁻¹)	k _{i,en} § (10 ⁻⁵ s ⁻¹)
(1,2)-ISOPOOH	0	7.4	0	2.0	1.0
(4,3)-ISOPOOH	0	11.8	0	2.0	1.0
MVK	0.2	2.0	5.2	0.2	1.0
MACR	0.3	2.8	1.2	0.2	1.0

^{*} Yields of the four products via isoprene ozonolysis were obtained from Master Chemical Mechanism v3.3.1 (30).

[†] For MVK and MACR, the reactions rate coefficients with OH or ozone were taken from IUPAC recommendation (48). For (1,2)-ISOPOOH and (4,3)-ISOPOOH, the reaction rate coefficients with OH were taken from St. Clair et al. (49), the reaction rate coefficients with ozone have not been reported yet and are hence taken as zero.

[‡] A deposition velocity of 2.0 cm s⁻¹ was used for ISOPOOH isomers, as recommended recently by Nguyen et al. based on measurements over a temperate forest (*50*). For MVK and MACR, the deposition rate was assumed to be one magnitude lower (i.e., 0.2 cm s⁻¹) considering its lower water solubility and reactivity.

An entrainment rate coefficient was determined by considering the entrainment velocity and concentration gradient between PBL and cloud layer. An entrainment velocity of 2.0 cm s⁻¹ was taken based on the simulated evolution of PBL height over a tropical forest during daytime (10:00-17:00 LT) (*43*). Based on reported vertical profiles of isoprene concentration and the ratio of the concentration of (MVK+MACR+ISOPOOH) to that of isoprene over central Amazonia (*22*, *23*), the concentration jump of MVK, MACR, and ISOPOOH between the PBL and the cloud layer is approximated by half of PBL concentration. Compared with a concentration jump of isoprene of one order of magnitude, the concentration jump of MVK, MACR, and ISOPOOH is smaller because of enhanced oxidation in the cloud layer (*22*, *23*).

Table S2: Uncertainty estimate for inferred $C_{OH,noon}$ via error propagation.

			Results at $\{C_{PROD}/C_{ISOP}, C_{NO_y} \text{ (ppb)}, t \text{ (h)}\}$			
			$\{0.4, 0.4, 7.5\}$	$\{0.7, 2.5, 8.5\}$	{1.2, 2.5, 9.5}	
Inferred value $C_{\rm OH,noon}(10^5{\rm cm}^{-3})$		6.7	9.1	20		
	x x	S_x				
Variable- specific	$C_{\rm PROD}/C_{\rm ISOP}$	15%	1.3	1.9	4.8	
<mark>error</mark>	$C_{\mathrm{NO}_{y}}$	<mark>20%</mark>	0.24	0.20	0.18	
$\left \frac{\partial G}{\partial x} \right S_x$	$\log(t^*_{ISOP})^*$	Log(2)	0.39	0.62	1.5	
$\frac{ \partial x }{(10^5 \text{ cm}^{-3})}$	$\left[\text{Log}(p_{\text{NO}_{\mathcal{Y}}, \text{yield}})^* \right]$	Log(1.5)	0.30	0.001	0.005	
	$\log(p_{\mathrm{OH},t})^*$	Log(2)	<mark>0.60</mark>	1.0	3.2	
Absolute standard error $S_{C_{OH,noon}}^{\dagger}$ (10 ⁵ cm ⁻³)		1.5	2.2	6.0		
Relative standard error $S_{C\mathrm{OH,noon}}/C_{\mathrm{OH,noon}}$		23%	25%	30%		

Error of respective variable follows lognormal distribution. The resultant variation of $C_{\text{ISOP}}(t)$, $y_i^*(C_{\text{NO}_y})$, and

 $C_{\text{OH}}(t)$ due to standard variation of t^*_{ISOP} , $p_{\text{NO}_{y,\text{yield}}}$ and $p_{\text{OH},t}$ is presented in Fig. S7 (a-c), respectively.

 † Standard error $S_{C_{\text{OH,noon}}}$ is estimated as square root of sum of squares of the variable-specific errors (cf. Eq. (S15)).

Table S3. Summary of inferred OH concentration over tropical rainforests in South America

Location & Time	Measurement	Methods	Inferred OH (cm ⁻³)	Ref.
Amazonia; wet season (1987)	Airborne (ABLE 2B)	Obs-constrained forward model	1.5× 10 ⁶ (daymax)	(45)
Suriname; wet season (1998)	Airborne (LBA-CLAIRE)	Obs-constrained forward model	$(1-3) \times 10^5 $ (24-h avg)	(46)
		Obs-constrained forward model	$(0.6-1.1) \times 10^6 (daymax)$	(47)
Amazonia; dry season (2001)	Airborne (LBA-CLAIRE)	Isoprene budget analysis	$(1-4) \times 10^6 \text{ (daytime)}$	(22)
		Vertical gradient of C_{PROD}/C_{ISOP}	$(3-8) \times 10^6 \text{ (daytime)}$	(22)
Amazonia; dry season (2004)	Airborne (TROFFEE)	Isoprene budget analysis	$(1.3 \pm 0.5) \times 10^6 \text{ (daytime)}$	(23)
		Vertical gradient of C_{PROD}/C_{ISOP}	$(4.3 \pm 2.4) \times 10^6$ (daytime)	(23)
Amazonia; wet season (2014)	Ground (GoAmazon 2014/5)	$C_{\mathrm{PROD}}/C_{\mathrm{ISOP}}$	$(0.5-1.2) \times 10^6 \text{ (daymax;}$ $IQR^*)$	This study
Amazonia; dry season (2014)	Ground (GoAmazon 2014/5)	$C_{ m PROD}/C_{ m ISOP}$	$(0.8-1.5) \times 10^6 \text{ (daymax;}$ $IQR^*)$	This study

^{*}IQR: inter-quartile range